

OPEN ACCESS

**Repository of the Max Delbrück Center for Molecular Medicine (MDC)  
in the Helmholtz Association**

<https://edoc.mdc-berlin.de/16425>

**Identification of a novel benzimidazole pyrazolone scaffold that inhibits  
KDM4 lysine demethylases and reduces proliferation of prostate cancer  
cells**

---

Carter, D.M., Specker, E., Przygodda, J., Neuenschwander, M., von Kries, J.P., Heinemann, U.,  
Nazaré, M., Gohlke, U.

This is the final version of the accepted manuscript. The original article has been published in final  
edited form in:

SLAS Discovery  
2017 AUG 1 ; 22(7): 801-812  
2017 MAR 27 (first published online)  
doi: [10.1177/2472555217699157](https://doi.org/10.1177/2472555217699157)

Publisher: [SAGE Publications](#)

Copyright © 2017 Society for Laboratory Automation and Screening

**Identification of a Novel Benzimidazole Pyrazolone Scaffold that Inhibits KDM4 Lysine Demethylases and Reduces Proliferation of Prostate Cancer Cells**

David M. Carter<sup>†</sup>, Edgar Specker<sup>‡</sup>, Jessica Przygodda<sup>†,‡</sup>, Martin Neuenschwander<sup>‡</sup>, Jens Peter von Kries<sup>‡</sup>, Udo Heinemann<sup>†</sup>, Marc Nazaré<sup>\*‡</sup>, Ulrich Gohlke<sup>\*†</sup>

<sup>†</sup>Max Delbrück Center for Molecular Medicine in the Helmholtz Association, 13125 Berlin, Germany

<sup>‡</sup>Leibniz-Institut für Molekulare Pharmakologie, 13125 Berlin, Germany

\*For M.N.; E-mail: nazare@fmp-berlin.de

\*For U.G.; E-mail: ulgohlke@zedat.fu-berlin.de

Abstract

Human lysine demethylase (KDM) enzymes (KDM1–7) constitute an emerging class of therapeutic targets, with activities that support growth and development of metastatic disease. By interacting with and co-activating the androgen receptor, the KDM4 subfamily (KDM4A–E) promotes aggressive phenotypes of prostate cancer (PCa); Knockdown of KDM4 expression or inhibition of KDM4 enzyme activity reduces the proliferation of PCa cell lines and highlights inhibition of lysine demethylation as a possible therapeutic method for PCa treatment. To address this possibility, we screened the ChemBioNet small molecule library for inhibitors of the human KDM4E isoform and identified several compounds with IC<sub>50</sub> values in the low micromolar range. Two hits, validated as active by an orthogonal ELISA-based assay, displayed moderate selectivity towards the KDM4 subfamily and exhibited anti-proliferative effects in cellular models of PCa. These compounds were further characterized for their ability to maintain the transcriptionally silent histone H3 tri-methyl K9 epigenetic mark at sub-cytotoxic

concentrations. Taken together, these efforts identify and validate a hydroxyquinoline scaffold and a novel benzimidazole pyrazolone scaffold as tractable for entry into hit-to-lead chemical optimization campaigns.

Keywords epigenetics, lysine demethylase (KDM), cancer, high-throughput screening (HTS)

## **Introduction**

Histone modifying enzymes facilitate the regulation of gene expression by mediating DNA accessibility. Methylation of specific lysine residues within histone tails by methyl transferase activity is known to down-regulate gene expression via formation of transcriptionally silent heterochromatin. Conversely, demethylation by lysine demethylase (KDM) enzymes activates gene transcription by initiating a process of chromatin decondensation which yields transcriptionally active euchromatin. To date, approximately twenty human KDM enzymes have been identified, each possessing the ability to demethylate mono-, di- or tri-methylated lysine residues within unstructured regions of histone tails. Together, these enzymes help regulate several disparate and coordinated cellular processes which function normally to maintain homeostasis and abnormally during the development of disease.

The Jumonji domain (Jmjd)-containing KDM4 subfamily comprises five functional members, KDM4A–E. Each isoform contains N-terminal catalytic Jumonji N- and C-domains that can demethylate di- and tri-methylated lysine 9 (KDM4A–E) and lysine 36 (KDM4A–C) of histone H3 (denoted H3K9/K36me<sub>2/3</sub>). Demethylation requires as co-substrates Fe<sup>2+</sup> and  $\alpha$ -ketoglutarate ( $\alpha$ -KG). Substrate turnover generates succinate, CO<sub>2</sub>, formaldehyde and demethylated H3K9/36 as products.

Since their discovery, KDM4 enzymes have been investigated for their ability to regulate pathways that culminate in metastatic disease. KDM4A–C isoforms are implicated<sup>1–5</sup> in aggressive phenotypes associated with metastatic prostate cancer (PCa). By associating with and co-activating<sup>2,3</sup> the androgen receptor (AR), these isoforms initiate a process of chromatin decondensation that renders AR-regulated gene promoters accessible for transactivation. Ultimately, this process enables PCa cells to grow and divide by expressing factors that give tumor cells selective growth advantage<sup>3</sup>. Initial experiments have demonstrated that knockdown of *KDM4C* gene expression reduced growth<sup>3</sup> of various PCa cell lines and suggested a novel therapeutic approach for treatment of this often lethal disease.

The extended Jmjd-containing KDM (Jmjd-KDM) superfamily is now recognized to play much wider roles in cancer biology and is implicated in supporting growth phenotypes of several disparate cancer lineages (reviewed in reference<sup>6</sup>). Given these broad and overlapping associations in cancer biology, KDM enzymes are increasingly found in chemical biology campaigns aimed at designing molecular probes which modulate their activity.

Several small molecules are described as inhibitors of Jmjd-KDMs (reviewed recently by McAllister *et al.*<sup>7</sup>). Most are analogs or structural mimics of  $\alpha$ -KG, and they inhibit the enzyme by interfering with co-substrate turnover. These inhibitors share structural determinants of binding with  $\alpha$ -KG, including  $\text{Fe}^{2+}$  chelation and formation of distal active-site hydrogen bonds.<sup>8</sup> Of these, the most characterized include N-oxalylglycine, as well as compounds bearing 8-hydroxyquinoline, 2,4-pyridine dicarboxylic acid and bipyridyl motifs.<sup>1,9–13</sup> In addition, a unique compound (JIB-04) was discovered<sup>14</sup> that non-competitively inhibits Jmjd-KDMs with respect to  $\alpha$ -KG.

These initial reports have fueled considerable interest in designing selective inhibitors of the Jmjd-KDM superfamily. Here, we report our efforts of screening for inhibitors of the human KDM4 family of lysine demethylase enzymes. By means of a formaldehyde dehydrogenase coupled-enzyme assay, we screened the ChemBioNet library (CBN)<sup>15</sup> for inhibitors of recombinant human KDM4E. As expected, some scaffolds were identified with motifs known to inhibit KDM4 enzymes. In addition, we identified several compound classes with unique chemistries that are as-of-yet undescribed. Inhibitory properties of the active compounds were confirmed by a novel enzyme-linked immunosorbent assay (ELISA) of KDM4E activity. Selectivity was examined by testing for inhibition against two representative enzymes from the extended superfamily of Jmjd-KDM enzymes. All members of the KDM4 subfamily were inhibited with similar potencies, highlighting the challenge of designing isoform-specific inhibitors should such a need arise. However, some selectivity was observed across the two distally related KDM enzymes of the Jmjd-KDM superfamily. Furthermore, select compounds elicited cytostatic responses in KDM4-expressing PCa cell lines including one compound that enriched levels of the H3K9me<sub>3</sub> epigenetic mark relative to untreated cells. Collectively, these compounds represent scaffolds with tractable features that are unexplored in published hit-to-lead campaigns.

### **Materials and Methods**

#### *Chemicals and Reagents*

Selected compounds of the ChemBioNet library (CBN IDs: 101848, 102735, 207192, 211191, 300553, 303229, 400447 and 402050) were purchased from Molport SIA (Riga, LV). The KDM4E inhibitor ML324 was purchased from ActiveMotif (Carlsbad, USA). Enzymology reagents ( $\alpha$ -ketoglutarate ( $\alpha$ -KG), sodium ascorbate, Fe(NH<sub>4</sub>)<sub>2</sub>(SO<sub>4</sub>)<sub>2</sub>, NAD<sup>+</sup> and TMB ELISA

substrate) were purchased from Sigma-Aldrich (St. Louis, USA). Antibodies were purchased from Thermo Fisher Scientific (Waltham, USA) (rabbit pAb H3K9me<sub>3</sub>, Invitrogen #49-1008), Abcam (Cambridge, UK) (mouse mAb H3K9me<sub>3</sub>, #ab6001 and rabbit pAb histone H3, #ab1791), BioVision (Milpitas, USA) (rabbit pAb histone H4, #3624-100) or Cell Signaling Technology (Danvers, USA) (HRP-mouse anti-rabbit IgG, #7074 or HRP-rabbit anti-mouse IgG, #7076).

#### *Plasmids, cDNA Clones and Enzymes*

cDNA clones encoding the catalytic domains of human KDM enzymes were purchased from Source Bioscience (Nottingham, UK). The catalytic domain of KDM4A (KDM4A<sub>cat</sub>) comprising residues 1-359 was cloned into the pQTEV expression vector containing an N-terminal hexahistidine tag. KDM4B<sub>cat</sub> (1-347) was cloned into the pET-28a expression vector and expressed as an N-terminal hexahistidine variant as previously described.<sup>4</sup> KDM4D<sub>cat</sub> (1-378) was cloned into the pNH-TrxT expression vector and expressed as a fusion protein bearing an N-terminal hexahistidine plus thioredoxin tag. KDM4C<sub>cat</sub> (1-347), KDM4E<sub>cat</sub> (1-337) and PHF8<sub>cat</sub> (Plant Homeodomain Finger protein 8, residues 115-483) were gifts from the Structural Genomics Consortium Oxford (Oxford, UK) and were expressed in *E. coli*, either as N-terminal hexahistidine variants from the vector pNic28-Bsa4 (KDM4C/E<sub>cat</sub>), or from pNH-TrxT (PHF8<sub>cat</sub>). The catalytic domain of KDM2A (1-517) was cloned into pQTEV and expressed as a hexahistidine variant. Formaldehyde dehydrogenase (FDH) from *Pseudomonas putida* was purchased from Sigma-Aldrich (St. Louis, USA).

#### *Enzyme Purification*

All KDM enzymes were purified by affinity and size exclusion chromatography as previously described (KDM2A,<sup>16</sup> KDM4A–E,<sup>4,9,17,18</sup> and PHF8<sup>19</sup>). With the exception of KDM4B, all constructs were processed by removal of N-terminal affinity tags prior to experimentation.

### *KDM Coupled-Enzyme Assay*

KDM activities were measured by a fluorescence-based coupled enzyme assay which measures reduction of NAD<sup>+</sup> to NADH by the coupling enzyme, formaldehyde dehydrogenase (FDH).<sup>20,21</sup> The assay used as KDM4A–E substrate a synthetic octapeptide (Biosyntan GmbH, Berlin, DE) corresponding to residues 8-15, AR-Kme<sub>3</sub>-STGGK, of histone H3 where (Kme<sub>3</sub>) represents tri-methylated lysine 9. A second peptide used as KDM2A/PHF8 substrate corresponded to residues 32-42, ATGGV-Kme<sub>2</sub>-KPHRY of histone H3, where (Kme<sub>2</sub>) represents di-methylated lysine 36. KDM4A–E were present at 1.5 μM, all other KDM enzymes were present at 2.0 μM. Details of the assay are described below in the *High-Throughput Screen* section. For validation studies, inhibition data were analyzed using a log[inhibitor] vs. normalized response model with variable slope as implemented in GraphPad Prism version 5.01 (Graphpad Software, La Jolla, USA).

### *High-Throughput Screen*

Screening was performed at the Screening Unit of the Leibniz-Institut für Molekulare Pharmakologie (FMP), Berlin. The ChemBioNet library was screened to identify inhibitors of KDM4E. The library comprised 32,032 small molecules that were curated based upon diverse chemical features represented in bioactive compounds of the World Drug Index.<sup>15</sup> During the primary screen, compounds were tested singly in 384-well microtiter plate (MTP) format analogous to previously reported screens against KDM4E.<sup>10,21</sup> The final assay was performed by first pipetting 10 μl of a 2-fold concentrated enzyme solution containing purified KDM4E and HEPES buffer into 368 wells of a 384-well MTP. Buffer alone was pipetted into the remaining 16 wells to serve as background controls. Compounds were then transferred (10 μM final concentration, 1% v/v final DMSO concentration) to each well, and the plate was incubated for 10 min at room temperature. Enzymatic reactions were initiated by adding 10 μl of 2-fold

substrate solution containing HEPES buffer, H3K9me<sub>3</sub> peptide, Fe(NH<sub>4</sub>)<sub>2</sub>(SO<sub>4</sub>)<sub>2</sub>, α-KG, sodium ascorbate, NAD<sup>+</sup> and FDH. Final assay conditions were: KDM4E (1.5 μM), H3K9me<sub>3</sub> (50 μM), Fe(NH<sub>4</sub>)<sub>2</sub>(SO<sub>4</sub>)<sub>2</sub> (40 μM), α-KG (1 mM), sodium ascorbate (2 mM), NAD<sup>+</sup> (1 mM), FDH (0.2 U/ml) and HEPES (20 mM, pH 7.5). Controls for DMSO-treated (1% v/v) enzyme and no-enzyme background (n=16, each) were included on each plate for calculation of Z'-factors<sup>22</sup> and to measure the robustness of screening. Initial velocities were measured over a period of 10 min from the increase in fluorescence due to FDH-coupled reduction of NAD<sup>+</sup> to NADH.

Fluorescence measurements ( $\lambda_{\text{ex}} = 355 \text{ nm}$ ,  $\lambda_{\text{em}} = 460 \text{ nm}$ ) were performed on a Safire 2 plate reader (Tecan Group Ltd., Männedorf, CH). Resulting initial velocities were used to calculate Z-scores for each reaction and to identify hits as statistical outliers from the distribution across all plates.<sup>22</sup> Finally, compounds were titrated to calculate IC<sub>50</sub> values as described in the Results section. As an initial validation of selected HTS hits, the FDH assay was employed in 96-well format using a FLUOstar Optima plate reader (BMG Labtech GmbH, Ortenberg, DE).

#### *KDM4 ELISA (CTH-ELISA)*

An orthogonal immunoassay was used as a secondary test to validate KDM4 inhibitors. The assay used as substrate core histones purified from calf thymus (CTH type II-A, Sigma-Aldrich, St. Louis, USA) and quantified directly the status of H3K9 tri-methylation. First, CTH were diluted into coating buffer (100 mM sodium carbonate, pH 8.0) to a final concentration of 0.02 μg/ml. Wells of a 96-well MTP were then coated with 1 μg CTH and incubated overnight at 4 °C with shaking. Wells designated as blanks were coated with buffer alone. The following day, plates were blocked for 2 h at 25 °C with blocking buffer (5% w/v) bovine serum albumin (BSA, AppliChem GmbH, Darmstadt, DE) in PBS (phosphate buffered saline) and washed 4 times for 5 min at 25 °C with ELISA wash buffer PBST (PBS plus 0.1% v/v Tween<sup>®</sup> 20). Wells were then



## Novel Scaffold Inhibitor of KDM4 Enzymes

conditioned by washing twice for 5 min with KDM reaction buffer (20 mM HEPES pH 7.5 plus 0.01% v/v Tween<sup>®</sup> 20). Meanwhile, KDM reaction components were prepared as 2-fold concentrated solutions containing a KDM4 isoform plus additives (HEPES, Fe(NH<sub>4</sub>)<sub>2</sub>(SO<sub>4</sub>)<sub>2</sub>, sodium ascorbate, Tween<sup>®</sup> 20). Concentrated enzyme mixtures were pre-diluted into water (100 μl 2-fold enzyme solution plus 46 μl H<sub>2</sub>O for each concentration of inhibitor tested). Inhibitor solutions dissolved in 100% DMSO were then added to enzyme mixtures (4 μl to each dilution of enzyme described above) and incubated on ice for 10 min prior to enzyme activation. Pure DMSO was added to enzyme mixtures in parallel as vehicle control. Enzymes were finally activated by a 1:4 dilution of a 4-fold solution containing concentrated α-KG. Final enzyme mixtures (200 μl) comprised: 100 nM KDM4 isoform in 20 mM HEPES pH 7.5, 10 μM Fe(NH<sub>4</sub>)<sub>2</sub>(SO<sub>4</sub>)<sub>2</sub>, 1 mM sodium ascorbate, 1 mM α-KG and 0.01% (v/v) Tween<sup>®</sup> 20. When applicable, DMSO was present at 2% (v/v).

Demethylation reactions were initiated by pipetting in triplicate, 50 μl of activated KDM4 solutions into appropriate wells of the CTH-coated MTP. Demethylation proceeded for 2 h at 37 °C. Plates were then washed 4 times for 5 min with PBST containing 1% (w/v) BSA (PBST-BSA). Levels of H3K9me<sub>3</sub> were detected by addition of primary antibody (rabbit, anti-human pAb to H3K9me<sub>3</sub>, Invitrogen, #49-1008) diluted 1:500 into blocking buffer and incubation of the plate for 60 min at 25 °C. Plates were then washed 4 times for 5 min with PBST-BSA before adding horseradish peroxidase (HRP)-coupled secondary antibody (mouse, anti-rabbit IgG, CST, #7074). Plates were incubated for 60 min at 25 °C, washed 4 times for 5 min with PBST-BSA and developed for 20 min at 25 °C by adding ELISA TMB substrate. Finally, reactions were quenched with 0.2 M H<sub>2</sub>SO<sub>4</sub> before reading the absorbance at 450 nm with a FLUOstar Optima plate reader. Raw values were corrected for background absorbance from blank wells, and the

percentage of H3K9me<sub>3</sub> remaining was expressed relative to wells containing 1 µg CTH. Data were analyzed with GraphPad Prism 5.01 as described above for the FDH-coupled enzyme assay.

#### *Cell Viability Assay*

Human prostate cancer cell lines (LnCaP, DU145 and PC-3) originated from ATCC and were maintained and propagated according to accompanied protocols. Cell viability was evaluated by the alamarBlue assay (Thermo Fisher Scientific, Waltham, MA) according to the manufacturer's protocol. The assay measures reduction of resazurin to resorufin in healthy cells. For all cell lines tested, 10,000 healthy cells were seeded into wells of an MTP (n = 6, for each test condition) and allowed to attach overnight at 37 °C, 5% CO<sub>2</sub>. Compounds were added the following day (0.5% final DMSO (v/v)) and incubated for 48 h prior to addition of the alamarBlue reagent. Presence of resorufin was detected by its fluorescence in a Tecan Infinite F200 Pro plate reader ( $\lambda_{\text{ex}} = 570$  nm,  $\lambda_{\text{em}} = 590$  nm). Percent viability was calculated as the ratio of fluorescence from wells containing cells  $\pm$  inhibitor relative to the fluorescence from wells containing cells grown in medium alone (healthy cell control) and was normalized relative to cell-free medium (dead cell control).

#### *Nucleosomal ELISA (Nu-ELISA)*

Global levels of methylated chromatin from cells grown in the presence of selected inhibitors or DMSO alone were measured by a Nu-ELISA, which quantifies a given epigenetic histone modification relative to a static control.<sup>23</sup> In our implementation, PCa cells (LnCaP, DU145 and PC-3 cell lines;  $5 \times 10^5$  cells each) were seeded into wells of a 6-well plate containing 2 ml of each respective growth medium. Cells were allowed to attach overnight at 37 °C, 5% CO<sub>2</sub>. The following day, culture medium was aspirated and replaced with test media: basal (growth

medium alone) or growth medium supplemented with KDM4 inhibitors (25  $\mu$ M ML324, 30  $\mu$ M CBN 207192, 100  $\mu$ M CBN 209350 or DMSO alone). The KDM4 inhibitor ML324 was used as a cell-permeable control.<sup>24</sup> Cells were then grown an additional 48 h under test conditions at which point medium was aspirated, cells washed twice with PBS, plates flash-frozen in liquid N<sub>2</sub> and stored overnight at -80 °C. The following day, plates were thawed at room temperature, and wells containing freshly lysed cells were resuspended in micrococcal nuclease (MNase) buffer as previously described.<sup>23</sup> Crude histone extracts were processed<sup>23</sup> by MNase digestion (Sigma-Aldrich, St. Louis, USA) and used to coat wells of a 96-well MTP. Plates containing the immobilized nucleosomal preparations were then blocked with BSA and probed for levels of the H3K9me<sub>3</sub> modification by addition of primary antibody (mouse, anti-human H3K9me<sub>3</sub>: Abcam #ab6001) diluted 1:100 in blocking buffer (5% (w/v) BSA in PBST). Second, identically-coated plates were probed for static levels of histone H4 (rabbit, anti-human histone H4: BioVision #3624) to serve as a loading control for normalization of H3K9me<sub>3</sub> levels detected in the first plate. Separate, identically-coated plates were also probed to evaluate levels of histone H3 (rabbit, anti-human histone H3: Abcam #ab1791) in order to assess whether growth conditions affected global levels of this histone. After a 60 min incubation at 25 °C, plates were washed, probed with HRP-conjugated secondary antibody and developed as described above for the KDM activity ELISA. The resulting colorimetric profiles from both plates were corrected by subtracting absorbance values from blank wells. Finally, signals arising from H3K9me<sub>3</sub> detection were expressed as a ratio relative to signals from identical wells of the paired plate that was probed with anti-H4 IgG. The resulting H3K9me<sub>3</sub>/H4 ratios were evaluated for statistical significance relative to DMSO-treated samples using a paired Student's *t*-test as implemented in Graphpad Prism 5.01.

## Results

### *Identification of Small Molecule Hits*

To initiate the HTS, we utilized a fluorescence-based and formaldehyde dehydrogenase-mediated coupled enzyme assay to measure inhibition of recombinant human KDM4E. The ChemBioNet small molecule library was then screened to search for novel KDM4E inhibitors. Global analysis<sup>25</sup> of the primary screen revealed it to be robust, with a mean  $Z'$  factor of  $0.7 \pm 0.2$  across all plates tested (**Fig. 1A**). The complete dataset therefore possessed statistical rigor needed to proceed with hit identification. For this, we employed a strategy that combined statistical scoring methods with a filtering scheme to exclude false positives (**Fig. 1B**). Of all compounds tested, 22 generated non-numeric initial velocities that likely arose from auto-fluorescent compounds which saturated the fluorescence detector during data acquisition. After omitting these compounds, 32,010 remained for further analysis. From these data, Z-scores were calculated<sup>22</sup> and plotted as a frequency distribution across the range of plates tested. A compound was designated as initial hit if its Z-score value was less than -3.5. Some compounds manifested as artifacts with apparent activities less than negative controls (samples without enzyme). To account for such potential false positives, samples with relative activity more than 20% below negative controls were omitted. Initially, 828 hits met the criteria for selection when present at a single concentration of 10  $\mu\text{M}$ . Of these, the 704 most active compounds were selected to validate KDM4E inhibition in duplicate (10  $\mu\text{M}$  compound concentration) and to screen for activity against the coupling enzyme, FDH. Cross-correlation analysis revealed compounds that favored inhibition of KDM4E over FDH (**Fig. 1C**); 550 compounds were found to inhibit FDH by more than 50% relative to controls and were omitted from further consideration. In total, 154 compounds were identified as KDM4E-specific inhibitors. These 154 compounds were selected

to calculate dose-dependent inhibition profiles against KDM4E and against FDH. Compounds were titrated in duplicate from 200 nM to 50  $\mu$ M, and the resulting inhibition profiles were fit to a four-parameter sigmoidal function to identify values of  $IC_{50}$  with IRLS robust regression methods using the software package Pipeline Pilot (Biovia, San Diego, USA). Compounds were then ranked by  $IC_{50}$  and examined for potential artifacts that could lead to their classification as false positive. Several compounds exhibited responses at high concentration indicative of assay interference due to their auto-fluorescence. We suspected that fluorescence from these compounds might contribute to the presumptive NADH fluorescence measured during data collection. To confirm this, we compared the fluorescence of each compound at 100  $\mu$ M in PBS (1% (v/v) DMSO) to an equimolar solution of NADH in PBS and to 100 nM solutions of fluorescein or rhodamine B in PBS. Of the 154 hits, nearly 75% were considered to be false positives based on comparisons between fluorescence profiles (**Suppl. Fig. S1**). By omitting these auto-fluorescent compounds, we focused on 47 final compounds (**Suppl. Tables S1, S2**) as primary hits for further validation and characterization. In addition to our identification of false positives, we recognize the possibility that the FDH enzyme used in the coupled enzyme assay has the potential to contribute as a source of false negatives. Commercial sources of this material are stabilized by bovine serum albumin at concentrations that can bind and sequester otherwise active molecules. With this caveat in mind, we did not explore whether albumin censors the available concentrations of molecules in the CBN library.

### *Characterization of Selected Hit Scaffolds*

Compounds designated as KDM4E inhibitors were further characterized by similarity and by known properties existing in curated databases. By clustering these hits into classes, we evaluated the chemical space selected during screening and rationalized whether the compounds

merit further investigation into a hit-to-lead campaign. Since optimization campaigns require significant resources, we defined essential properties of an ideal hit. At this stage of the screening process, we sought hits that could inhibit KDM4 enzymes in a competitive manner. We avoided compounds that could irreversibly inhibit enzymes as they might not possess the selectivity required to target KDM4 in living cells. Furthermore, we focused on compounds that were neither over-represented as hits from in-house databases nor from curated online databases. Such frequent hitters may arise due to assay interference (PAINS compounds) and could complicate downstream analyses. Finally, we focused on compounds with scaffolds that are suitable for derivatization in order to gain insight into the structure-activity relationship (SAR) at an early stage.

Classification of the chemical space selected during the HTS resulted primarily in the clusters outlined in **Supplemental Table S1**. Most clustered either as quinones (Class A) or catechols/chelators of iron (Class B). Quinones are known for reactive proclivity towards protein thiols and were not considered for further analysis. Hits classified either as catechols or as those bearing motifs known to scavenge metals were also omitted from further consideration due to the possibility that simple  $\text{Fe}^{2+}$  scavenging accounted for their inhibitory effect. Compounds in several other classes were also eliminated from further consideration given that they were either prone to oxidation (Class C), too large for optimization (Class D), designated as frequent hitters (Classes E and F) or decorated with more than one nitro group (Class G).

Eight compounds were identified as singletons and could not be assigned to any group. These hits were therefore grouped together into an orphan class (**Suppl. Table S2**). Of these, we excluded compound CBN 102502, from further consideration due to the possibility of acting as

Fe<sup>2+</sup> scavenger and compounds CBN 203240 and CBN 401835 due to the detection of additional masses in samples taken from the HTS library.

### *Validation of Selected Hits*

After the initial assessment of HTS hit properties, we identified eight classes of compounds considered tractable for follow-up analysis (**Suppl. Table S3**). Compounds from each of these eight classes were either purchased from commercial vendors, or synthesized and validated as active: first by the FDH-coupled fluorescence assay and second by a novel CTH-ELISA. Most of the compounds were eventually classified as false positives for several reasons. For example, the purchased compounds CBN 211191, 400447 and 402050 were all found to be highly autofluorescent in the confirmatory FDH assay. Compounds CBN 101848 and CBN 102735 were both found to be inactive after re-synthesis or after re-purification of purchased material (102735). Finally, the piperidinyl methanamine class of compounds was either inactive in orthogonal enzyme assays (CBN 300553) or was unstable in aqueous solution (CBN 303229). Given these outcomes, false positive compounds were omitted from further consideration.

Listed in **Table 1** are the remaining two HTS hits assessed for validation. Prior to this, we assessed each compound for purity. Analytical LC-MS experiments revealed compound CBN 207192 to be approximately 75% pure, while CBN 209350 was found to be nearly 100% pure (**Suppl. QC data**). Both inhibit KDM4E in the low micromolar range and also meet relevant descriptors such as the Lipinski rules (**Suppl. Table S4**), and they were therefore considered tractable for validation. Importantly, we identified CBN 207192 which bears a hydroxyquinoline motif known to inhibit Jmjd-KDM enzymes.<sup>10,11</sup> Identification of this hit therefore validated our screening strategy and strengthened our interpretation that hits of interest were not false positives. The second compound, CBN 209350, represents a novel scaffold with chemistry that is

as-of-yet undescribed in literature describing KDM inhibition. In confirmatory fluorescence assays (**Fig. 2A**), values of  $IC_{50}$  for both compounds generally agreed with those measured during the primary screen (**Table 1**). In contrast, the coupling enzyme formaldehyde dehydrogenase, was inhibited to a lesser extent (**Fig. 2B**).

We further employed an ELISA-based method as a second and independent measure of inhibition which directly measures the methylation status of a core histone substrate. Similar to the confirmatory fluorescence-based assay, both HTS hits were generally found to be active by ELISA (**Fig. 2C; Table 1**). Excellent agreement between  $IC_{50}$  values from the fluorescence assay and ELISA were obtained for compound CBN 207192, whereas 209350 exhibited an approximately 100-fold weaker  $IC_{50}$  value by the ELISA. However, 209350 repeatedly yielded unique bi-phasic inhibition curves in both the fluorescence assay and the ELISA (**Suppl. Fig. S2**). When the CTH-ELISA data were fit to a bi-phasic inhibition model, a lower  $IC_{50}$  value of 12.5  $\mu$ M was evident (in agreement with the FDH assay), followed by a weaker inhibitory phase (apparent  $IC_{50} = 800 \mu$ M) (**Suppl. Fig. S2**). The reason for this discrepancy remains a topic for further investigation.

#### *KDM Selectivity*

Employing the FDH-coupled fluorescence assay and the CTH-ELISA, validated compounds were tested for selectivity within members of the KDM4 family and across two distal members of the Jmjd-KDM superfamily. Values of  $IC_{50}$  indicate that these compounds were not selective within the KDM4 isoform subfamily (**Suppl. Table S5**). Similar results were obtained by the CTH-ELISA; All KDM4 isoforms were inhibited to similar degrees when tested at identical single inhibitor concentrations (**Fig. 2D**). These results are not surprising given the high degree of sequence similarity between catalytic domains of this family. However, moderate selectivity



was observed against two distal members of the extended Jmjd KDM superfamily. This appeared highest for compound CBN 209350 ( $IC_{50}$  [KDM4] = 4-8  $\mu$ M), which inhibited KDM2A with an  $IC_{50}$  of 120  $\mu$ M and PHF-8 with an  $IC_{50}$  of 30  $\mu$ M (**Fig. 2E,F; Suppl. Table S5**). Whether these compounds exhibit selectivity across the entire superfamily of Jmjd-KDMs remains to be determined.

#### *Cell-Based Activities of Validated Hit Scaffolds*

We next tested whether validated compounds were active against human PCa model cell lines, including those that overexpress KDM4A/C (LnCaP, DU145 and PC-3 cell lines).<sup>2,26,27</sup> All cell lines exhibited cytostatic responses at high inhibitor concentrations (**Fig. 3A–C; Table 1**). Compound CBN 207192 was consistently the most potent compound tested, whereas 209350 generally displayed cytostatic effects at higher concentrations (> 500  $\mu$ M). Of the PCa cell lines tested, PC-3 cells exhibited the weakest inhibitory response. The complete ChemBioNet library has also been profiled using standard assay settings for cell viability testing to assess the cytotoxicity of each compound against two standard non-cancer cell lines: HEK293 and HepG2 (unpublished data). From these data, compound CBN 207192 exhibited some toxicity against the non-cancer HEK293 cell line, but not against the HepG2 cell line (data not shown). Conversely, CBN 209350 was not found to be toxic to either cell line. This might reflect a generally greater cytostatic potential for CBN 207192. However, since we aim to inhibit KDM4 enzymes, we consider that differences in cytostatic properties could be due to differences in KDM4-dependent growth phenotypes, as well as the amount of KDM4 isoform expressed relative to each cell line.

#### *Methylation Status of Chromatin from Inhibitor-Treated Cells*

Finally, we tested whether cytostatic effects observed in the cell-based assays correlated with an increase in global levels of methylated chromatin. The recently described Nu-ELISA technique

enables direct quantification of dynamic epigenetic modifications relative to a static normalizing chromatin motif.<sup>23</sup> For this study, we compared dynamic levels of the H3K9me<sub>3</sub> mark relative to levels of a static sequence derived from the N-terminus of histone H4. Crude preparations of chromatin from cells grown in basal medium, medium plus DMSO (vehicle control), or medium plus KDM4 inhibitors were processed into nucleosomal units by addition of the enzyme micrococcal nuclease. KDM4 inhibitor concentrations were chosen based on results from cell proliferation assays. We selected concentrations (30 μM CBN 207192 and 100 μM CBN 209350) that did not compromise cell viability, but which approached or exceeded the values of IC<sub>50</sub> measured by the *in vitro* FDH assay (24 μM and 4 μM, respectively).

As a cell-permeable control, we used the published KDM4 inhibitor, ML324 (IC<sub>50</sub> against KDM4E = 29 μM, data not shown), which has been suggested to modulate global levels of chromatin methylation by inhibiting KDM4 enzymes.<sup>24</sup> Methylation of H3K9 was quantified by an ELISA with a primary antibody that specifically detects the H3K9me<sub>3</sub> modification. These values were normalized to an identical plate which was probed for static levels of histone H4. Normalized levels of H3K9me<sub>3</sub> from cells grown in test conditions were compared relative to cells grown in basal medium plus DMSO.

Chromatin methylation levels profiled by this approach are depicted in **Figure 3**. Global levels of the H3K9me<sub>3</sub> epigenetic mark remained unchanged in LnCaP and DU145 cell lines grown in the presence of 0.5% (v/v) DMSO relative to cells grown in basal medium alone (**Fig. 3D, E**). Treatment with 25 μM ML324 caused a significant increase in H3K9 methylation relative to treatment with DMSO in both LnCaP and DU145 cell lines. Similar results were observed when these cells were grown in the presence of 30 μM CBN 207192, whereas treatment with 100 μM 209350 did not alter chromatin methylation. By contrast, these same

treatments yielded markedly different results in the PC-3 cell line (**Fig. 3F**). This cell line exhibited a highly significant decrease in H3K9 methylation when treated with DMSO alone. Interestingly, both ML324 and 209350 appeared to cause a further decrease in methylation in the PC-3 cell lines compared to DMSO. However, similar to LnCaP and DU145 cell lines, treatment of PC-3 cells with 207192 caused a highly significant increase in H3K9 methylation compared to DMSO. This increase was also significant relative to H3K9me<sub>3</sub> levels of PC-3 cells grown in basal medium ( $p=0.0195$ ). In parallel, we tested whether fluctuations in global levels of histone H3 accounted for the changes observed in epigenetic levels of H3K9me<sub>3</sub> (**Suppl. Fig. S3**). We considered that Histone H3 is not an ideal candidate for use as a normalizing motif since it is known to exist as an ensemble of three differentially expressed isoforms and is highly homologous to centromere protein A (CENPA), all of which are detectable by histone H3-specific antibodies. Whereas H3 levels were mostly unaffected, they were significantly different from basal conditions for DU145 cells grown in the presence of both ML324 and 207192 (apparent decreases) and for PC-3 cells grown in the presence of 209350 (apparent increase). However, these differences are small and are not expected to influence the H3K9me<sub>3</sub>/H4 ratios described above, especially given the opposing effects such differences would be expected to exert on the magnitude of the ratio. Taken together, these results indicate that treatment of PCa cell lines with membrane-permeable compounds ML324 (LnCaP and DU145 cell lines) and 207192 (LnCaP, DU145 and PC-3 cell lines) resulted in increased levels of H3K9 methylation compared to cells grown in culture medium alone. This outcome is expected if KDM enzymes are inhibited. Reduced levels of H3K9 methylation from PC-3 cells grown in the presence of DMSO, ML324 or 209350 possibly indicate a unique response to cytotoxic challenge compared to the other cell lines tested. In addition, given the relatively high concentration of inhibitors

used in our cell-based assays, we recognize that off-target effects may also contribute to the observations discussed above.

## Discussion

The discovery that KDM enzymes promote cancer cell growth has prompted several campaigns focusing on inhibitor development and the therapeutic potential that lies therein. Here we describe the identification of two scaffolds that inhibit members of the Jmjd-KDM enzyme superfamily. We validated our HTS campaign as successful by identifying CBN 207192 which bears a scaffold known to inhibit KDM4 isoforms. We also provide initial evidence for selectivity of the benzimidazole pyrazolone scaffold for the KDM4 family of isoforms and demonstrate that both HTS hits exhibit anti-cancer effects by reducing the proliferation of PCa cell lines. These results highlight the promise of compounds 207192 and 209350 as interesting candidates for further investigation by structural and biochemical methods and possibly for immediate entry into hit-to-lead campaigns.

Compound CBN 207192 contains the well-characterized 8-hydroxyquinoline (8-HQ) motif known to chelate iron in the KDM4A active site. Crystal structures of this fragment bound to KDM4A (PDB ID 3NJY, 4BIS) revealed how the motif chelates active site iron.<sup>10,11</sup> The substituted ring position observed in 207192 opposes that reported from other 8-HQ inhibitors, revealing a relatively unexplored region for further modification. It most closely resembles a piperazine-substituted 8-HQ inhibitor developed by Schofield and colleagues (PDB ID 3RVH). These similarities suggest that 207192 might chelate the metal center within the KDM4 active site if the hydroxyquinoline ring flips its orientation relative to that observed in the crystal structures noted above (**Fig. 4A, B**). Furthermore, if 207192 chelates iron in this orientation, its piperazine ring might still contact the enzyme as observed in PDB 3RVH.

We conclude that the novel KDM4 inhibitor CBN 209350 exhibits features most intriguing for further investigation. First, the compound represents a scaffold with properties that are as-of-yet undescribed in KDM inhibitors. Second, the compound is active in orthogonal enzyme assays and exhibits some specificity towards KDM4 enzymes. Third, it displays cytostatic activity in PCa cell lines at higher concentration. Fourth, it bears key structural similarities (**Fig. 4C**) to other privileged scaffolds which inhibit Fe<sup>2+</sup>/α-KG-dependent hypoxia inducible factor prolyl hydroxylase (PHD) enzymes such as the drugs Molidustat<sup>28</sup> and a benzimidazole-2-pyrazole carboxylate described by Rosen and colleagues<sup>29</sup>. Finally, we suggest that its mode of binding (**Fig. 4D**) reflects those observed in crystal structures of a KDM2A-specific inhibitor (triazolopyridine) bound to KDM4A (PDB ID 4URA), of a pyrazolopyridine inhibitor bound to KDM4A (PDB ID 4GD4), or of a diazole inhibitor bound to KDM5B (PDB ID 5FPL).<sup>30</sup> A secondary binding mode observed in a crystal structure containing a benzimidazole fragment bound to the surface of KDM4D (PDB ID 4D6S) may also apply to 209350.

These most tractable scaffolds are active across orthogonal assays of KDM activity. Our use of the CTH-ELISA is advantageous in its simplicity and requires no specialized equipment. Materials used in the assay are familiar to most laboratories, and several measurements of IC<sub>50</sub> values are easily performed in a single day. A possible limitation of the assay is the need to work with well-characterized antibodies. We found that results varied with the commercial source of antibody used, indicating an essential need to characterize the antibody prior to use in such experiments. Despite this drawback, we obtained excellent agreement between IC<sub>50</sub> values for compound CBN 207192.

Compound CBN 209350 was unique in that the  $IC_{50}$  calculated from the CTH-ELISA was a hundred times larger than that observed from the fluorescence assay. We are still investigating the source of this discrepancy, but it may result from what we identified as a bi-modal response in the inhibition profiles. When these data from both assays are fit to a bi-modal inhibition model, we observe two values for  $IC_{50}$ : a high-affinity value of around 12  $\mu$ M, and a low-affinity value of around 800  $\mu$ M. It is possible that fluorescence-based assays are more sensitive to measurements of the higher-affinity binding site where artifacts due to ligand fluorescence are less substantial.

Anti-proliferative properties of the compounds in the KDM4-expressing PCa cell lines generally agreed with the KDM4E inhibition profiles generated by CTH-ELISA. Compound CBN 207192 was most cytostatic towards PCa cells, followed by 209350. We expected that compounds exerting a cytostatic response in PCa cells mediate their effects at least in part through inhibition of intracellular KDM4 enzymes. The resulting Nu-ELISA profiles from cell lines treated with the cell-permeable KDM4 inhibitor ML324 and our HTS hit CBN 207192 provide some evidence to support this hypothesis. Chromatin methylation profiles from LnCaP and DU145 cells were similar; both exhibited significant increases in the H3K9me<sub>3</sub> mark when treated with either compound. Conversely, we were unable to detect significant changes in methylation when these cells were treated with 209350 possibly reflecting hindered passage across the cell membrane. Calculation of physicochemical properties by the SwissADME server ([www.swissadme.ch](http://www.swissadme.ch)) reveals (**Suppl. Table S4**) that compound 209350 has a larger polar surface area (PSA) (87.7 Å<sup>2</sup>) and smaller clogP value (1.20) relative to 207192 (PSA 59.8 Å<sup>2</sup> and clogP 2.71, respectively). These properties may render 209350 less permeable to cell membranes which could account for the observation that all cell lines tolerated higher concentrations of the

compound. Alternatively, hydrolysis of the methylester moiety by intracellular esterases might render the compound less active in living cells. The contrasting results obtained for the PC-3 cell line are more difficult to reconcile. Our results suggest that this cell line may respond to cytotoxic challenges in a different manner than LnCaP and DU145 cells. Whereas all cell lines used in this study derive from prostate carcinomas, they represent metastatic states of disease which arise from unique trajectories of biological selection and transformation.

We now aim to evaluate the potential of these selected scaffolds in optimization campaigns. In particular, we will evaluate structure-activity-relationships around the benzimidazole pyrazolone scaffold of CBN 209350, to characterize it more thoroughly by enzyme kinetics, to assess its selectivity across a larger panel of Jmjd-KDM enzymes and to elucidate its mode of binding by determining crystal structures of KDM4-inhibitor complexes. We anticipate that such structural details will help clarify our observation of bi-phasic inhibition curves. Additionally, whether this and derivatives of the same chemotype inhibit cell growth by targeting KDM4 enzymes within the cellular milieu will be further investigated. Use of quantitative real-time PCR, reporter gene assays, and chromatin methylation profiling technologies will be of considerable value with such investigations. Ultimately, we believe that these efforts will generate useful tool compounds for probing epigenetic modifications in cell biology, and that they will contribute towards new therapeutic approaches to treat malignancies such as prostate cancer.

## **Acknowledgments**

This work was supported by an MDC GO-Bio grant awarded to DC. We would like to recognize the talented and valuable contributions by M. Schneider and V. Schwietzke for help in cloning and purifying various KDM enzymes. We would also like to thank G. Illing for influential contributions and support during the conceptual phase of the project.

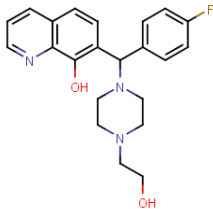
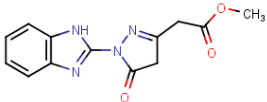


## References

1. Cloos, P. A. C.; Christensen, J.; Agger, K.; et al. The Putative Oncogene GASC1 Demethylates Tri- and Dimethylated Lysine 9 on Histone H3. *Nature* **2006**, *442*, 307–311.
2. Shin, S.; Janknecht, R. Activation of Androgen Receptor by Histone Demethylases JMJD2A and JMJD2D. *Biochem. Biophys. Res. Commun.* **2007**, *359*, 742–746.
3. Wissmann, M.; Yin, N.; Müller, J. M.; et al. Cooperative Demethylation by JMJD2C and LSD1 Promotes Androgen Receptor-Dependent Gene Expression. *Nat. Cell Biol.* **2007**, *9*, 347–353.
4. Chu, C.-H.; Wang, L.-Y.; Hsu, K.-C.; et al. KDM4B as a Target for Prostate Cancer: Structural Analysis and Selective Inhibition by a Novel Inhibitor. *J. Med. Chem.* **2014**, *57*, 5975–85.
5. Coffey, K.; Rogerson, L.; Ryan-Munden, C.; et al. The Lysine Demethylase, KDM4B, Is a Key Molecule in Androgen Receptor Signalling and Turnover. *Nucleic Acids Res.* **2013**, *41*, 4433–4446.
6. Song, Y.; Wu, F.; Wu, J.; et al. Targeting Histone Methylation for Cancer Therapy: Enzymes, Inhibitors, Biological Activity and Perspectives. *J. Hematol. Oncol.* **2016**, *9*, 49.
7. McAllister, T. E.; England, K. S.; Hopkinson, R. J.; et al. Recent Progress in Histone Demethylase Inhibitors. *J. Med. Chem.* **2016**, *59*, 1308–29.
8. Alam, H.; Gu, B.; Lee, M. G. Histone Methylation Modifiers in Cellular Signaling Pathways. *Cell. Mol. Life Sci.* **2015**, *72*, 4577–92.
9. Rose, N. R.; Ng, S. S.; Mecinović, J.; et al. Inhibitor Scaffolds for 2-Oxoglutarate-Dependent Histone Lysine Demethylases. *J. Med. Chem.* **2008**, *51*, 7053–7056.
10. King, O. N. F.; Li, X. S.; Sakurai, M.; et al. Quantitative High-Throughput Screening Identifies 8-Hydroxyquinolines as Cell-Active Histone Demethylase Inhibitors. *PLoS One* **2010**, *5*, e15535.
11. Hopkinson, R. J.; Tumber, A.; Yapp, C.; et al. 5-Carboxy-8-Hydroxyquinoline Is a Broad Spectrum 2-Oxoglutarate Oxygenase Inhibitor Which Causes Iron Translocation. *Chem. Sci.* **2013**, *4*, 3110–3117.
12. Schiller, R.; Scozzafava, G.; Tumber, A.; et al. A Cell-Permeable Ester Derivative of the JmjC Histone Demethylase Inhibitor IOX1. *ChemMedChem* **2014**, *9*, 566–571.
13. Feng, T.; Li, D.; Wang, H.; et al. Novel 5-Carboxy-8-HQ Based Histone Demethylase JMJD2A Inhibitors: Introduction of an Additional Carboxyl Group at the C-2 Position of Quinoline. *Eur. J. Med. Chem.* **2015**, *105*, 145–155.
14. Wang, L.; Chang, J.; Varghese, D.; et al. A Small Molecule Modulates Jumonji Histone Demethylase Activity and Selectively Inhibits Cancer Growth. *Nat. Commun.* **2013**, *4*, 2035.
15. Lisurek, M.; Rupp, B.; Wichard, J.; et al. Design of Chemical Libraries with Potentially Bioactive Molecules Applying a Maximum Common Substructure Concept. *Mol. Divers.* **2010**, *14*, 401–408.
16. Cheng, Z.; Cheung, P.; Kuo, A. J.; et al. A Molecular Threading Mechanism Underlies Jumonji Lysine Demethylase KDM2A Regulation of Methylated H3K36. *Genes Dev.* **2014**, *28*, 1758–71.

17. Ng, S. S.; Kavanagh, K. L.; McDonough, M. A.; et al. Crystal Structures of Histone Demethylase JMJD2A Reveal Basis for Substrate Specificity. *Nature* **2007**, *448*, 87–91.
18. Krishnan, S.; Trievel, R. C. Structural and Functional Analysis of JMJD2D Reveals Molecular Basis for Site-Specific Demethylation among JMJD2 Demethylases. *Structure* **2013**, *21*, 98–108.
19. Yue, W. W.; Hozjan, V.; Ge, W.; et al. Crystal Structure of the PHF8 Jumonji Domain, an Nepsilon-Methyl Lysine Demethylase. *FEBS Lett.* **2010**, *584*, 825–30.
20. Lizcano, J. M.; Unzeta, M.; Tipton, K. F. A Spectrophotometric Method for Determining the Oxidative Deamination of Methylamine by the Amine Oxidases. *Anal. Biochem.* **2000**, *286*, 75–79.
21. Sakurai, M.; Rose, N. R.; Schultz, L.; et al. A Miniaturized Screen for Inhibitors of Jumonji Histone Demethylases. *Mol. Biosyst.* **2010**, *6*, 357–364.
22. Brideau, C.; Gunter, B.; Pikounis, B.; et al. Improved Statistical Methods for Hit Selection in High-Throughput Screening. *J. Biomol. Screen.* **2003**, *8*, 634–647.
23. Dai, B.; Giardina, C.; Rasmussen, T. P. Quantitation of Nucleosome Acetylation and Other Histone Posttranslational Modifications Using Microscale NU-ELISA. *Methods Mol. Biol.* **2013**, *981*, 167–76.
24. Rai, G.; Kawamura, A.; Tumber, A.; et al. Discovery of ML324, a JMJD2 Demethylase Inhibitor with Demonstrated Antiviral Activity; *Probe Reports from the NIH Molecular Libraries Program Bethesda (MD)*. **2010**.
25. Zhang, J.-H. A Simple Statistical Parameter for Use in Evaluation and Validation of High Throughput Screening Assays. *J. Biomol. Screen.* **1999**, *4*, 67–73.
26. Duan, L.; Rai, G.; Roggero, C.; et al. KDM4/JMJD2 Histone Demethylase Inhibitors Block Prostate Tumor Growth by Suppressing the Expression of AR and BMYB-Regulated Genes. *Chem. Biol.* **2015**, *22*, 1185–1196.
27. Kim, T.-D.; Jin, F.; Shin, S.; et al. Histone Demethylase JMJD2A Drives Prostate Tumorigenesis through Transcription Factor ETV1. *J. Clin. Invest.* **2016**, *126*, 706–720.
28. Flamme, I.; Oehme, F.; Ellinghaus, P.; et al. Mimicking Hypoxia to Treat Anemia: HIF-Stabilizer BAY 85-3934 (Molidustat) Stimulates Erythropoietin Production without Hypertensive Effects. *PLoS One* **2014**, *9*, e111838.
29. Rosen, M. D.; Venkatesan, H.; Peltier, H. M.; et al. Benzimidazole-2-Pyrazole HIF Prolyl 4-Hydroxylase Inhibitors as Oral Erythropoietin Secretagogues. *ACS Med Chem Lett.* **2010**, *1*(9), 526–529.
30. Bavetsias, V.; Lanigan, R. M.; Ruda, G. F.; et al. 8-Substituted Pyrido[3,4-D]pyrimidin-4(3H)-One Derivatives As Potent, Cell Permeable, KDM4 (JMJD2) and KDM5 (JARID1) Histone Lysine Demethylase Inhibitors. *J. Med. Chem.* **2016**, *59*, 1388–1409.

**Table 1.** Inhibition profiles of validated KDM4 inhibitors.

		KDM4 Inhibitor - ChemBioNet ID			
		207192	209350		
					
HTS	FDH Assay	IC <sub>50</sub> , μM	5	11	
	Validation	FDH Assay	IC <sub>50</sub> , μM	24	4
95% C.I. <sup>a</sup>			23 – 26	4 – 5	
Top <sup>a</sup>			94%	103%	
Bottom <sup>a</sup>			2%	2%	
Hill Slope <sup>a</sup>			-1.8	-0.8	
Residual <sup>b</sup>		11%	6%		
CTH ELISA		IC <sub>50</sub> , μM	28	581 <sup>c</sup>	
		95% C.I. <sup>a</sup>	23 – 33	486 – 696	
		Top <sup>a</sup>	82%	100%	
		Bottom <sup>a</sup>	9%	0%	
	Hill Slope <sup>a</sup>	3.3	0.8		
Residual <sup>b</sup>	18%	10%			
Cell Viability	LnCaP	IC <sub>50</sub> , μM	130	410	
		95% C.I. <sup>a</sup>	116 – 137	375 – 449	
		Top <sup>a</sup>	96%	101%	
		Bottom <sup>a</sup>	0%	0%	
		Hill Slope <sup>a</sup>	-3.2	-1.5	
	Residual <sup>b</sup>	2%	15%		
	DU145	IC <sub>50</sub> , μM	290	>1000	
		95% C.I. <sup>a</sup>	198 – 416	NA <sup>d</sup>	
		Top <sup>a</sup>	97%	NA <sup>d</sup>	
		Bottom <sup>a</sup>	0%	NA <sup>d</sup>	
		Hill Slope <sup>a</sup>	-1.3	NA <sup>d</sup>	
	Residual <sup>b</sup>	3%	69%		
	PC-3	IC <sub>50</sub> , μM	350	>1000	
		95% C.I. <sup>a</sup>	208 – 600	NA <sup>d</sup>	
		Top <sup>a</sup>	106%	NA <sup>d</sup>	
Bottom <sup>a</sup>		0%	NA <sup>d</sup>		
Hill Slope <sup>a</sup>		-1.1	NA <sup>d</sup>		
Residual <sup>b</sup>	1%	79%			

<sup>a</sup>95% confidence interval (in units of μM) from best fits of data to inhibition model (n = 3); Top and Bottom refer to upper and lower limits of enzyme activity/cell viability from the mono-phasic inhibition model; Hill Slope refers to the slope of the best fit line to the inhibition model.

<sup>b</sup>Percent residual enzyme activity or cell viability at highest inhibitor concentration tested

<sup>c</sup>Values of IC<sub>50</sub> = 12.5 μM and 800 μM when fit to a bi-phasic inhibition model.

<sup>d</sup>Not applicable due to curve fitting results

## Figure Legends

**Figure 1.** High-throughput screening workflow. **(A)** Distribution of initial screen  $Z'$ -factors across all plates tested. The mean  $Z'$ -factor is represented by the dotted horizontal line. **(B)** Schematic depicting HTS workflow and data processing strategies. See the Results sections for a detailed description. **(C)** Cross-correlation plot of KDM4E vs. FDH Inhibition. Cross-correlation analysis was used to identify HTS hits as defined by compounds that inhibit KDM4E with between -10% to 60% activity (“relative activity” between -0.1 and 0.6) and which inhibit the coupling enzyme (FDH) no more than 50% (“relative activity”  $> 0.5$ ). Data points fitting these criteria lie within the boundaries of the depicted rectangle and constitute the 154 hits described in the main text.

**Figure 2.** Validation of selected KDM4E inhibitors. Selected HTS primary hits were either purchased or synthesized and re-tested for inhibition by orthogonal assays of KDM4E activity. **(A)** KDM4E inhibition profiles determined by the FDH-coupled fluorescence assay. **(B)** Counter-screen depicting inhibition profiles of the coupling enzyme, formaldehyde dehydrogenase (FDH). **(C)** KDM4E inhibition profiles determined by the CTH-ELISA. **(D)** CTH-ELISA inhibition profiles of 50  $\mu$ M CBN 207192 (blue bars) and 500  $\mu$ M CBN 209350 (red bars) tested against members of the KDM4 family. **(E)** KDM2A inhibition profiles determined by the FDH-coupled fluorescence assay. **(F)** PHF8 inhibition profiles determined by the FDH-coupled fluorescence assay. Inhibition data from compounds are depicted in all panels as follows: 207192 (blue squares), 209350 (red circles). Error bars in all plots represent mean  $\pm$  SEM from three independent replicates.

**Figure 3.** Activities of KDM4 inhibitors in cellular models of prostate cancer. **(A–C)** Cell viability profiles of validated HTS hits. Cell lines [LnCaP **(A)**]; DU145 **(B)**]; or PC-3 **(C)**] were

grown to near confluence and challenged with increasing concentrations of KDM4 inhibitors. Treated cells were then incubated for an additional 48 h and analyzed for viability by the alamarBlue assay. Inhibitor treatments in panels A-C are represented as follows: CBN 207192 (blue squares), CBN 209350 (red circles). Error bars represent mean  $\pm$  SEM from six independent replicates. **(D–F)** Comparison of global H3K9me<sub>3</sub> levels from treated cell cultures. Cell lines [LnCaP, panel **(D)**; DU145, panel **(E)**; PC-3, panel **(F)**] were grown in untreated culture medium (basal) or medium supplemented with either 0.5% DMSO or inhibitory compounds (25  $\mu$ M ML324, 30  $\mu$ M 207192 or 100  $\mu$ M 209350). After a 48 h growth period under test conditions, cells were washed, lysed and treated with micrococcal nuclease to obtain crude nucleosomal preparations. Boxes represent ratios of H3K9me<sub>3</sub> signals relative to histone H4 signals from cells grown under paired test conditions. Error bars represent mean  $\pm$  SEM from nine independent replicates. Statistical significance of test conditions relative to DMSO were evaluated by a paired Student's *t*-test: **(D)** LnCaP cells (ML324 \*\**p*=0.0091; 207192 \*\**p*=0.0028); **(E)** DU145 cells (ML324 \*\*\**p*<0.001; 207192 \*\**p*=0.0013); **(F)** PC-3 cells (DMSO \*\*\**p*<0.001; ML324 \**p*=0.0171; 207192 \*\*\**p*=0.0002, 209350 \*\**p*=0.0018). Data which were not significantly different in *t*-test comparisons with respect to DMSO are denoted in the figure as “ns”.

**Figure 4.** Molecular models of KDM4 inhibitors. **(A,B)** Models of hydroxyquinoline compounds bound to KDM4A. Cross-sections of KDM4A's active site are examined from the crystal structure of PDB 3RVH. Depicted in **(A)** is a bound hydroxyquinoline piperazine-based inhibitor as determined by Schofield and colleagues. Compound CBN 207192 is manually docked to 3RVH in panel **(B)**. KDM4A residues that make canonical H-bonds with  $\alpha$ -KG and/or inhibitors are depicted in yellow stick representation. Active site Fe<sup>2+</sup> is depicted as orange spheres. The

fluorobenzyl ring of 207192 is obscured by a protrusion of KDM4A's active site. **(C)** Drugs that target  $\text{Fe}^{2+}/\alpha\text{-KG}$ -dependent enzymes with molecular scaffolds similar to CBN 209350. **(D)** Proposed binding mode of CBN 209350. KDM4A's  $\alpha\text{-KG}$ -bound active site is represented as observed in the crystal structure PDB 2GP5. Outlined in red is the region occupied by bound  $\alpha\text{-KG}$ . Compound CBN 209350 (cyan stick representation) was manually positioned into the KDM4A active site by constraining metal-inhibitor interactions that occur in known KDM4-inhibitor structures. Canonical H-bond-forming residues Lys206 and Tyr132 are depicted in yellow stick representation and labeled accordingly. The region of space within KDM4A's active site which becomes occupied by the histone H3 methyl-Lys sidechain is depicted as a red triangle. Protein modeling and figure generation were performed with the PyMOL Molecular Graphics System, Version 1.6 Schrödinger, LLC.

**Figure 1.** High-throughput screening workflow.

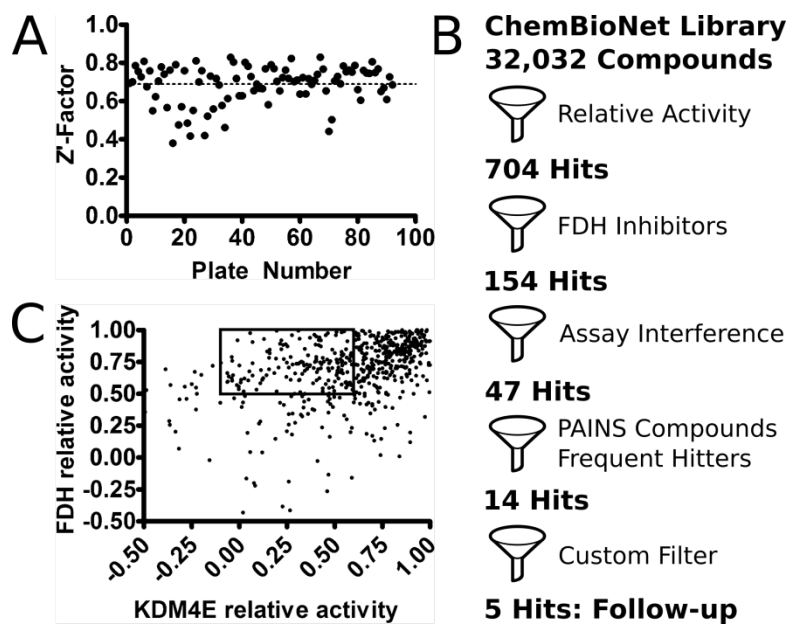


**Figure 2.** Validation of KDM4E inhibitors.

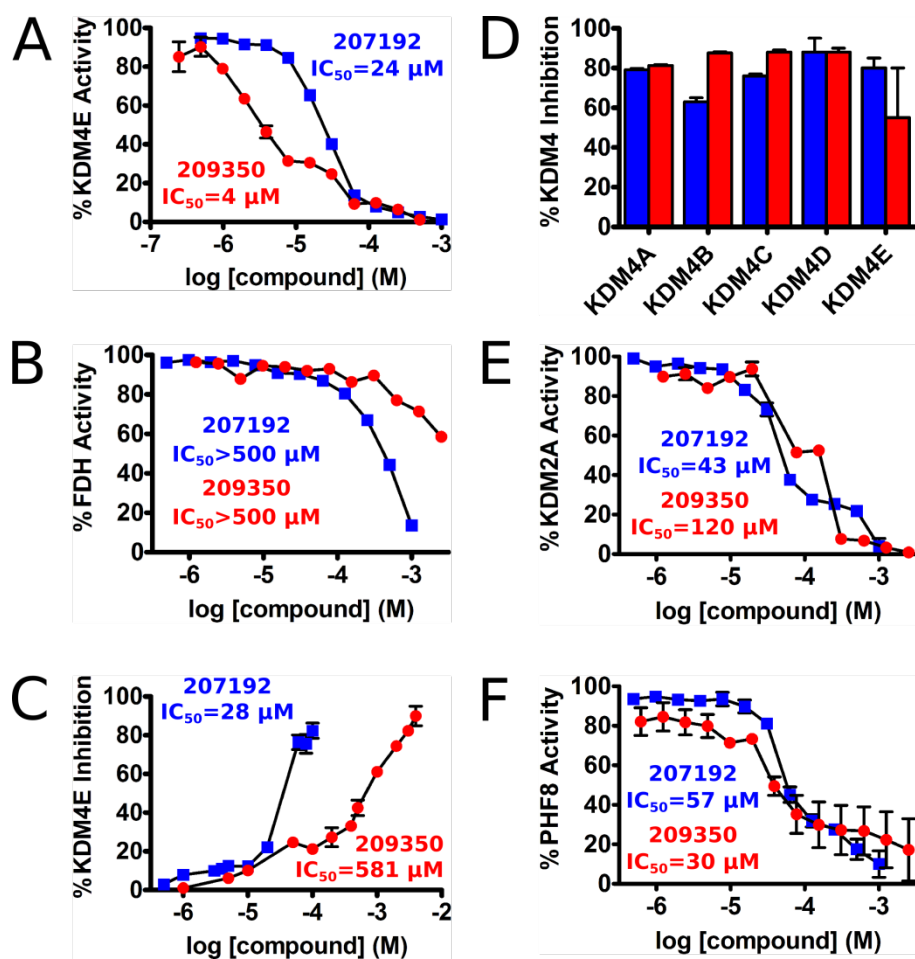




**Figure 3.** Activities of KDM4 inhibitors in cellular models of prostate cancer.

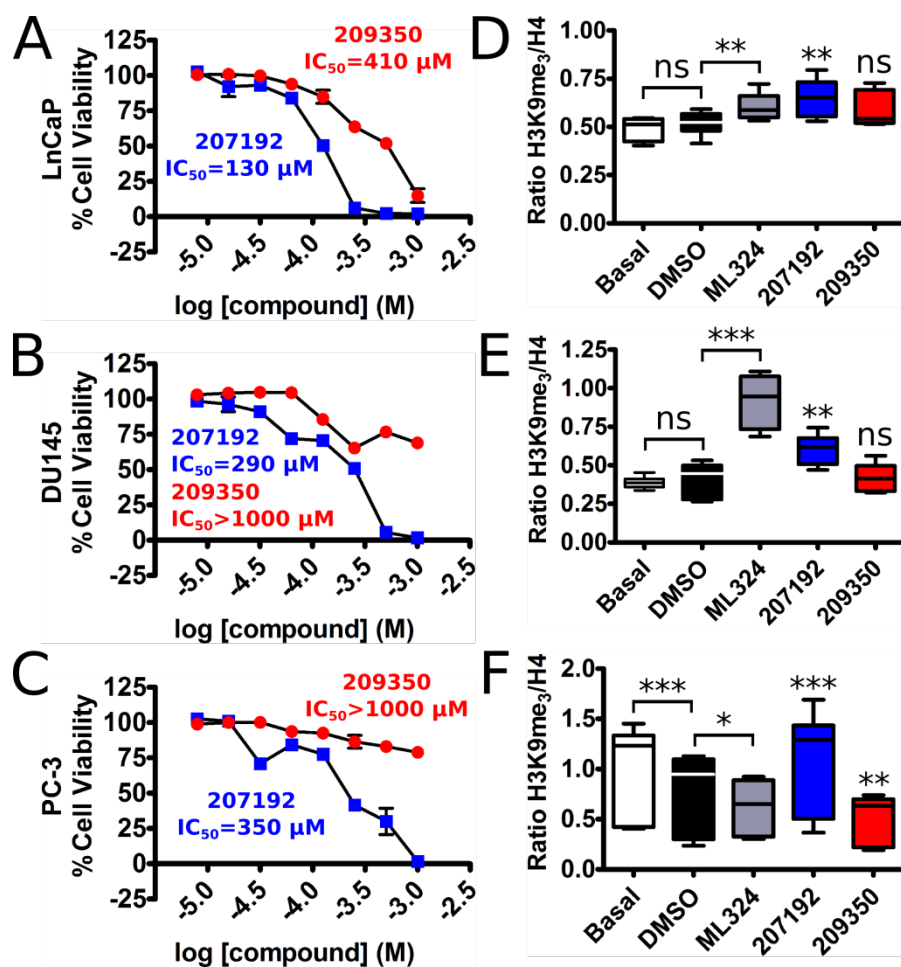
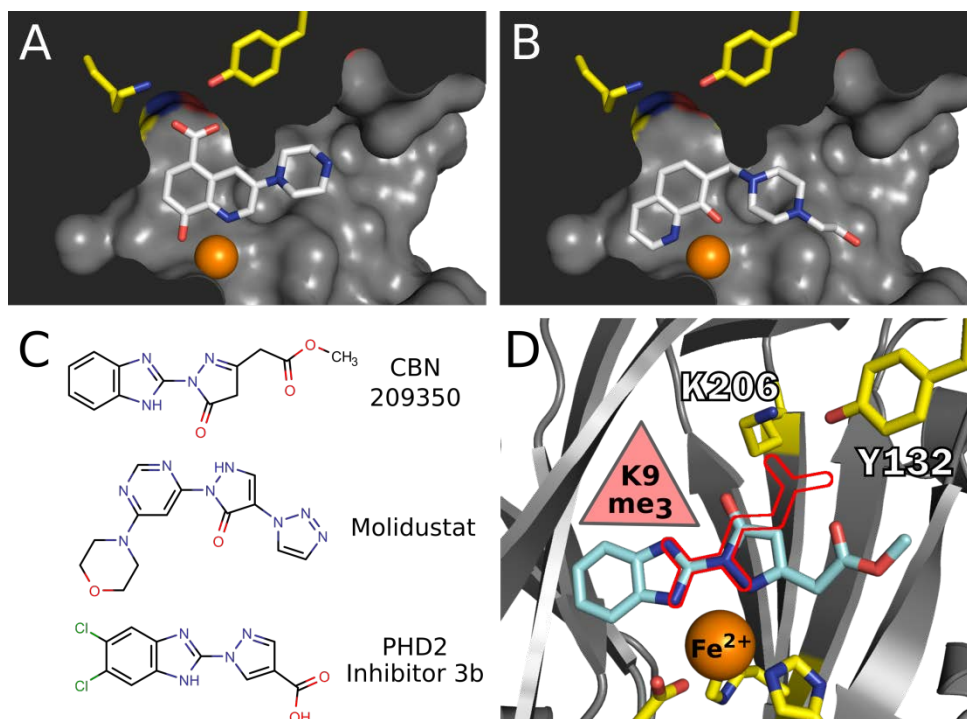


**Figure 4.** Molecular modeling of KDM4–inhibitor interactions.



## **Supplementary Information**

**for**

### **Identification of a Novel Benzimidazole Pyrazolone Scaffold that Inhibits KDM4 Lysine Demethylases and Reduces Proliferation of Prostate Cancer Cells**

David M. Carter<sup>†</sup>, Edgar Specker<sup>‡</sup>, Jessica Przygodda<sup>†,‡</sup>, Martin Neuenschwander<sup>‡</sup>, Jens Peter von Kries<sup>‡</sup>, Udo Heinemann<sup>†</sup>, Marc Nazaré<sup>\*‡</sup>, Ulrich Gohlke<sup>\*†</sup>.

<sup>†</sup>Max Delbrück Center for Molecular Medicine in the Helmholtz Association, 13125 Berlin, Germany

<sup>‡</sup>Leibniz-Institut für Molekulare Pharmakologie, 13125 Berlin, Germany

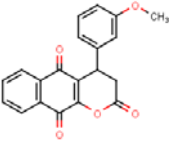
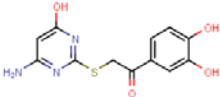
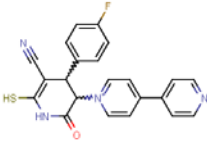
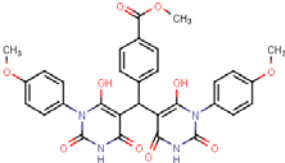
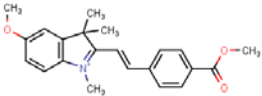
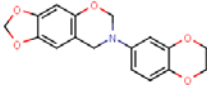
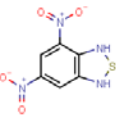
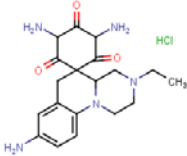
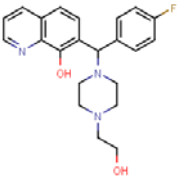
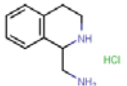
\*For M.N.; E-mail: nazare@fmp-berlin.de

\*For U.G.; E-mail: ulgohlke@zedat.fu-berlin.de

#### **Contents:**

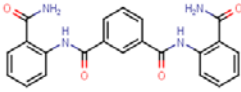
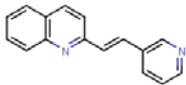
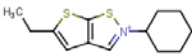
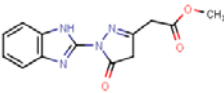
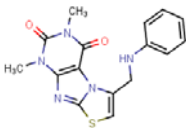
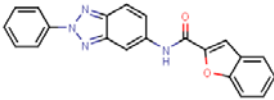
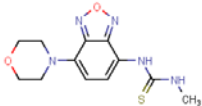
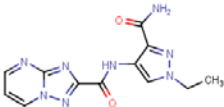
**Supplemental Tables S1-S5, Supplemental Figures S1-S3, Supplemental Methods, Quality Control Data and Supplemental References**

**Table SI.** Chemical Classification of Primary HTS Hits

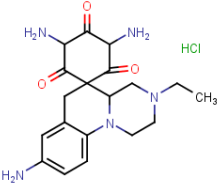
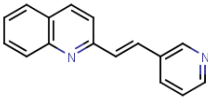
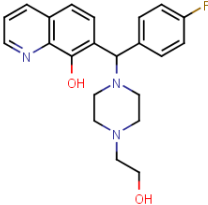
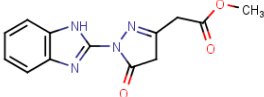
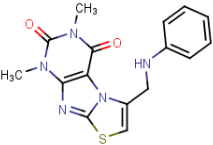
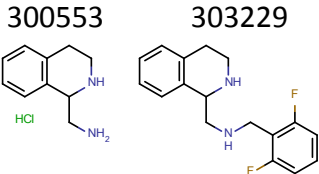
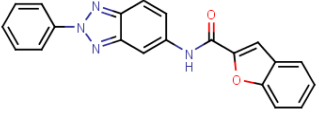
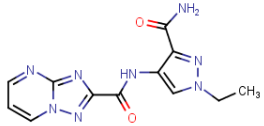
Compound Class	CBN IDs	Scaffold	Example Structure	IC <sub>50</sub> Range, $\mu$ M
A	101238 200006	quinones		7 – 42
	200400 200420			
	203105 210577			
	211346 211347			
B	102620 200475	catechols / iron chelators		8 – 33
	200477 206533			
	209295 209465			
	209668 216379			
C	101500	linear bipyridyl ring-conjugates		11 – 14
	101508			
	103171			
D	207155	pyrimidine trione substitutions		7 – 11
	210538			
	400759			
E	202953	indole substitutions		6 – 16
	202959			
	207539			
F	200150	benzodioxole substitutions		2 – 36
	404127			
G	201631 304018	nitro-compounds		26 – 30
H	101848	spiropiperazines		3 – 5
	101859			
	101870			
	101907			
I	206849	hydroxyquinoline derivatives		5 – 26
	207192			
	300683			
J	300553	piperidinyl methanamines		10 – 25
	303229			

Novel Scaffold Inhibitor of KDM4 Enzymes

**Table S2.** Orphan Class of Primary HTS Hits

CBN ID	Scaffold	Structure	IC <sub>50</sub> , μM	%Residual Activity at Highest Concentration
102502	linked benzamide		10	25
102735	quinoline substitution		7	0
203240	thieno-thiazole		3	0
209350	benzimidazole pyrazolone		10	50
211191	pyrimidine dione		10	0
400447	benzotriazole substitution		20	0
401835	benzofurazan		10	10
402050	pyrazole carboxamide		6	25

**Table S3.** HTS Hit Classes Selected for Validation Studies

CBN ID	Scaffold	Structure(s) <sup>a</sup>	IC <sub>50</sub> , μM <sup>b</sup>	Validation Results	Final Assessment
<b>101848</b> 101859 101870 101907	spiropiperazines		3 – 5	Inactive after re-synthesis	False Positive
<b>102735</b>	pyridylquinoline		3	Inactive after re-synthesis	False Positive
206849 <b>207192</b> 300683	hydroxyquinoline derivatives		5 – 26	Active	Valid KDM4 Inhibitor
<b>209350</b>	benzimidazole pyrazolone		11	Active	Valid KDM4 Inhibitor
<b>211191</b>	pyrimidinedione		10	Highly Fluorescent	False Positive
<b>300553</b> <b>303229</b>	piperidinyll methanamines		19 – 23	Inactive in orthogonal assay (300553) Unstable in aqueous solution (303229)	False Positives
<b>400447</b>	substituted benzotriazole		20	False Positive	False Positive
<b>402050</b>	pyrazole carboxamide		6	False Positive	False Positive

<sup>a</sup>Structures are depicted for compounds whose CBN ID numbers are highlighted in bold<sup>b</sup>Ranges calculated from fitting of HTS data to inhibition model

**Table S4.** Physicochemical Properties<sup>a</sup> of Validated HTS Scaffolds

Scaffold	CBN ID	M <sub>r</sub> (g/mol)	#H-bond donors	#H-bond acceptors	partition coefficient (clogP)	polar surface area (Å <sup>2</sup> )
hydroxyquinoline	207192	381.44	2	6	2.71	59.83
benzimidazole pyrazole	209350	272.26	1	5	1.20	87.65

<sup>a</sup>Properties calculated by the SwissADME server ([www.swissadme.ch](http://www.swissadme.ch))

**Table S5.** KDM Isoform Inhibition Data

HTS		Validation				
CBN ID	IC <sub>50</sub> , μM	Enzyme	IC <sub>50</sub> , μM	95% C.I. <sup>a</sup>	%Residual Activity <sup>b</sup>	ELISA
207192	5.2	KDM2A	43.0	36.7 – 50.4	31%	Not Determined
		KDM4A	34.8	32.8 – 36.9	11%	Active
		KDM4B	25.3	23.9 – 26.7	12%	Active
		KDM4C	26.2	24.4 – 28.1	13%	Active
		KDM4D	27.6	25.1 – 30.4	18%	Active
		KDM4E	24.4	22.7 – 26.2	11%	Active
		PHF8	56.5	47.0 – 67.9	36%	Not Determined
		FDH	>500	695 - 2488	84%	Not Determined
209350	10.7	KDM2A	120.2	75.1 – 192.3	54%	Not Determined
		KDM4A	8.2	6.8 – 9.8	12%	Active
		KDM4B	7.0	6.0 – 8.2	9%	Active
		KDM4C	6.6	5.5 – 7.8	9%	Active
		KDM4D	8.0	6.4 – 10.0	9%	Active
		KDM4E	4.1	3.5 – 4.9	6%	Active
		PHF8	30.4	13.3 – 69.6	33%	Not Determined
		FDH	>500	Very Wide	91%	Not Determined

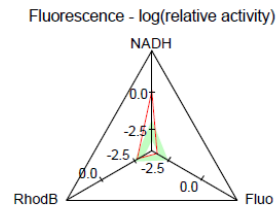
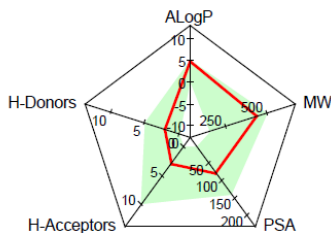
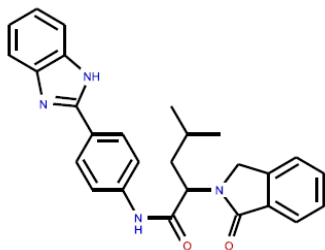
<sup>a</sup>95% Confidence interval (in μM) from curve fitting analysis

<sup>b</sup>Percent residual activity remaining at 100 μM inhibitor concentration

## Novel Scaffold Inhibitor of KDM4 Enzymes

[Link\\_to\\_PubChem for compound 201307](#)  
ChemDiv-E612-0829

Position on plate: F19



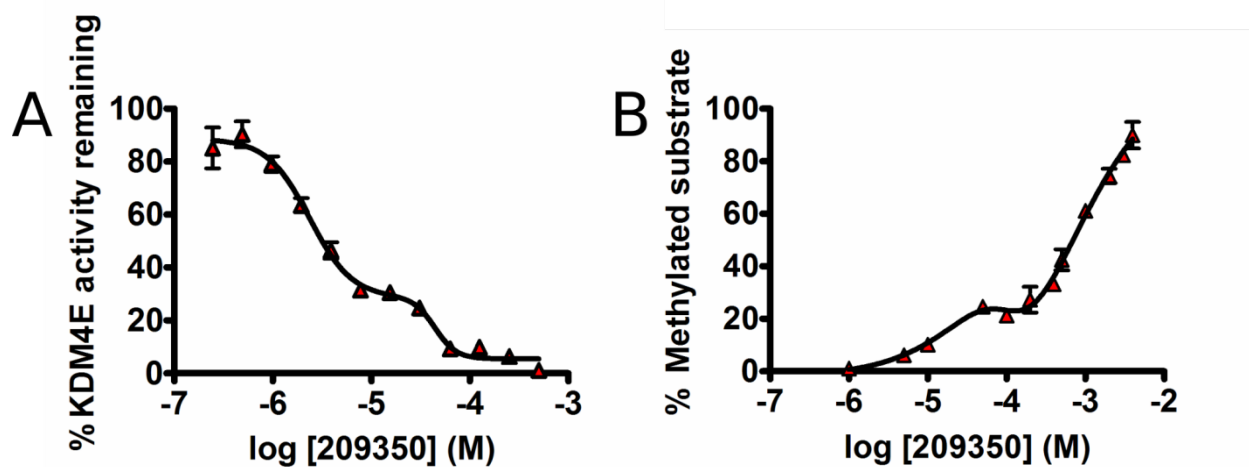
Properties	Specificity
Solubility: Clear solution at 20 mM in DMSO: true  Purity: no MS data available  Fluorescence: 100uM NADH: 121.7% 0.1uM Fluorescein: 0.0% 0.1uM Rhodamin B: 0.2%	(inhibitors/activators) of all_measured:  (0/0) of 4 in general_cell (0/0) of 7 in alphascreeen (0/0) of 4 in elisa (0/1) of 2 in HTRF (0/0) of 7 in firefly (0/0) of 9 in general_biochemical (1/0) of 3 in LabChip (0/0) of 1 in FluoPol (0/0) of 1 in cAMP  (1/1) of 38 in total



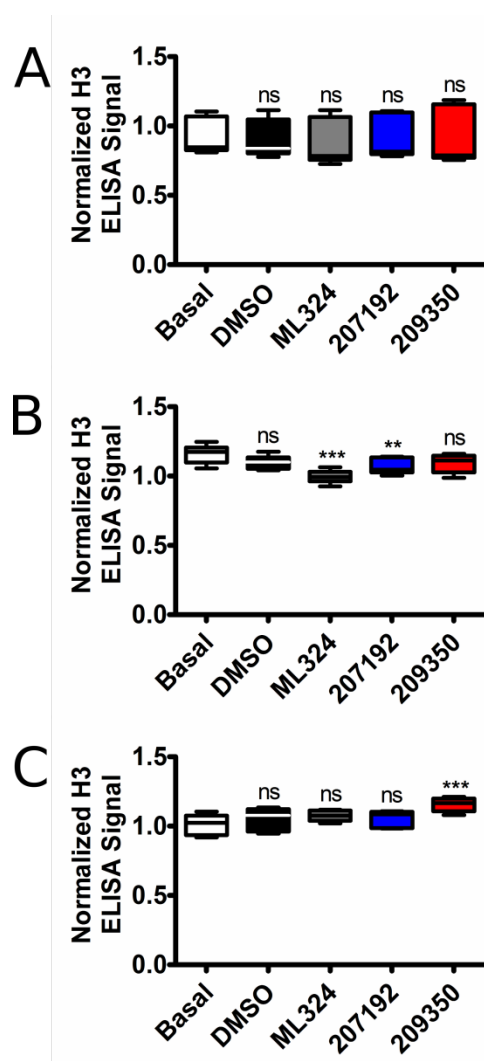
Appearance 10 mM in DMSO

**Supplemental Figure S1.** Example of a false-positive HTS hit with spectral properties that interfere with assay signal. In this example, the compound exhibits 21.7% greater fluorescence than an equimolar concentration of NADH in PBS (depicted in radar plot (top right) and properties box (bottom left)).





**Supplemental Figure S2.** Data from HTS hit CBN 209350 re-fit to a bi-phasic inhibition model in Graphpad Prism. **(A)** Data from the FDH assay. **(B)** Data from the CTH-ELISA. Best fit lines are illustrated in black. Error bars represent mean  $\pm$  SEM from three independent replicates.



**Supplemental Figure S3.** Nu-ELISA data for histone H3. Chromatin from cells grown under the conditions depicted was analyzed for total histone H3 content using an antibody specific for H3 (Abcam ab1791). Differences in H3 signals between cells grown under basal (medium alone) versus test conditions (n=9 each) were assessed for statistical significance by Student's *t*-tests as implemented in Graphpad Prism 5.01: **(A)** Nu-ELISA histone H3 profiles for LnCaP cells. (ns: not significant) **(B)** Nu-ELISA histone H3 profiles for DU145 cells. (ns: not significant; \*\*\*:  $p < 0.0001$  ; \*\*:  $p = 0.0044$ ) **(C)** Nu-ELISA histone H3 profiles for PC-3 cells (ns: not significant; \*\*\*:  $p = 0.0001$ ).

## Supplemental Methods

### Chemical Synthesis

Procurement of selected HTS primary hits for validation studies proceeded either by purchase of commercially available materials or by synthesis (spiropiperazine, hydroxyquinoline, benzimidazole pyrazolone and pyridylquinoline scaffolds). Synthesis of precursors provided insight about stability of the final hit scaffold and allowed general access to a variety of synthesizable derivatives.

LCMS (method 2): Instrument: Agilent Technologies 6120 Quadrupole LC/MS linked to Agilent Technologies HPLC 1290 Infinity; Column: Thermo Accuore RP-MS; Particle Size: 2.6  $\mu$ M Dimension: 30 x 2.1 mm; Eluent A: H<sub>2</sub>O with 0.1% TFA Eluent B: MeCN with 0.1% TFA; Gradient: 0.00 min 95% A, 0.2 min 95% A, 1.1 min 1% A, 2.5 min Stoptime, 1.3 min Posttime; Flow rate: 0.8 ml/min; UV-detection: 220 nm, 254 nm, 300 nm. Purification of the compounds by chromatography was achieved using a CombiFlash Rf 200 UV-VIS System from Axel Semrau®. Preparative HPLC-method: Instrument: Waters Prep 150 LC System ChromScope v. 1.4; Column: Machery-Nagel VP 250 x 21 mm Nucleodur® 100-7 C18 ec; Eluent A: H<sub>2</sub>O with 0.1% TFA Eluent B: MeCN with 0.1% TFA; Gradient: 0.00 min 85% A, 2 min 85% A, 22 min 15% A, 24 min 15% A, 26 min 0% A, 29 min 0% A, 32 min 85% A; Flow rate: 30 ml/min; UV-detection: 254 nm

Hydroxyquinolines were synthesized in a one-pot Betti reaction using 8-hydroxyquinoline, benzaldehyde and substituted piperazines with catalytic amounts of formic acid.<sup>2</sup> First, an imine was formed via condensation of an aldehyde and a piperazine, followed by addition of formic acid and hydroxyquinoline.

### 1,3-Dimethyl-5-(5-nitro-2-(piperazin-1-yl)benzylidene)pyrimidine-2,4,6(1H,3H,5H)-trione

Spiropiperazines were synthesized in two steps starting from *tert*-butyl 4-(2-formyl-4-nitrophenyl)piperazine-1-carboxylate and *N,N*-dimethyl barbituric acid to yield  $\alpha,\beta$ -unsaturated 5-arylmethylidenebarbituric acids via an aldol-condensation.<sup>1</sup> In the second step, a Michael acceptor functionality was exploited to cyclize the scaffold to the spiropiperazine in boiling acetic acid.

335.4 mg (1 mmol) of *tert*-butyl 4-(2-((1,3-dimethyl-2,4,6-trioxotetrahydropyrimidin-5(2H)-ylidene)methyl)-4-nitrophenyl)piperazine-1-carboxylate was solubilized in 10 ml EtOH and stirred at 50 °C. 1,3-Dimethylbarbituric acid (156.14 mg, 1 mmol) solubilized in 4 ml EtOH/H<sub>2</sub>O (60/40) was added to the mixture and stirred for 5 min. The mixture was cooled to RT and stirred for 1 h. The product precipitated as yellow powder and was filtered off as raw material. It was washed twice with EtOH and H<sub>2</sub>O and dried under reduced vacuum. Raw product was suspended in 4 M HCl in dioxane and stirred at RT for 2 h. Solvent was removed under reduced pressure and the product was isolated as HCl salt. Yield (335 mg, 90%).

<sup>1</sup>H NMR (300 MHz, DMSO-*d*<sub>6</sub>) δ 8.65 (d, *J* = 2.7 Hz, 1H), 8.27 (dd, *J* = 9.1, 2.8 Hz, 1H), 8.13 (s, 1H), 7.32 (d, *J* = 9.1 Hz, 1H), 3.34 (s, 6H), 3.27 (s, 4H), 3.19 (s, 4H). LCMS: *R*<sub>t</sub> = 3.10 min; MS (ESIpos) *m/z* = 274.00 [M+H]<sup>+</sup>

3-Acetyl-1',3'-dimethyl-8-nitro-2,3,4,4a-tetrahydro-1H,2'H,6H-spiro[pyrazino[1,2-a]quinoline-5,5'-pyrimidine]-2',4',6'(1'H,3'H)-trione

55 mg (0.15 mmol) of 1,3-dimethyl-5-(5-nitro-2-(piperazin-1-yl)benzylidene)pyrimidine-2,4,6(1*H*,3*H*,5*H*)-trione was suspended in 20 ml acetic acid and stirred at 100 °C under reflux for 16 h. Solvent was removed under reduced pressure and the raw product precipitated in 4 ml of ether, filtered off and washed a few times with ether (Yield: 59 mg, 96%).

<sup>1</sup>H NMR (300 MHz, DMSO-*d*<sub>6</sub>) δ 7.96 (dd, *J* = 9.2, 2.8 Hz, 1H), 7.89 (s, 1H), 7.03 (d, *J* = 9.4 Hz, 1H), 4.21 - 4.03 (m, 2H), 4.03 - 3.92 (m, 1H), 3.84 - 3.62 (m, 1H), 3.58 - 3.41 (m, 2H), 3.37 - 3.25 (m, 3H), 3.18 (s, 3H), 3.12 - 3.05 (s, 3H), 1.95 (s, 3H). LCMS: *R*<sub>t</sub> = 6.74 min; MS (ESIpos) *m/z* = 416.11 [M+H]<sup>+</sup>

(E)-2-(2-(Pyridin-3-yl)vinyl)quinoline

The pyridylquinoline scaffold was prepared by condensation between 2-methylquinoline and 3-pyridinecarboxaldehyde in acetic anhydride. The resulting pyridylvinlyquinoline was reduced with H<sub>2</sub> and Pd/C to the 2-(2-(pyridin-2-yl)ethyl)quinolone.<sup>5,6</sup>

215 mg (1.5 mmol) 2-methylquinoline was solubilized in 1.5 ml acetic anhydride followed by addition of 3-pyridinecarboxaldehyde. The mixture was stirred at 100 °C under reflux for 16 h. Solvent was removed under reduced pressure, and the crude product was purified by chromatography on silica gel eluting with a gradient of hexane/EtOAc (Yield: 266 mg, 76%).

<sup>1</sup>H NMR (300 MHz, chloroform-*d*) δ 8.84 (d, *J* = 2.4 Hz, 1H), 8.57 (dd, *J* = 4.8, 1.7 Hz, 1H), 8.26 (d, *J* = 8.5 Hz, 2H), 8.06 – 8.00 (m, 1H), 7.84 (dd, *J* = 8.1, 1.4 Hz, 1H), 7.81 – 7.72 (m, 3H), 7.66 (s, 1H), 7.61 – 7.55 (m, 1H), 7.36 (dd, *J* = 8.0, 4.7 Hz, 1H). LCMS: R<sub>t</sub> = 2.95 min; MS (ESIpos) *m/z* = 233.15 [M+H]<sup>+</sup>.

#### 2-(2-(pyridin-3-yl)ethyl)quinoline

50 mg (0.22 mmol) of (E)-2-(2-(pyridin-3-yl)vinyl)quinoline was solubilized in 2 ml THF in a microwave vial. 2.29 mg of Pd/C was added followed by purging of the vial with H<sub>2</sub>. The mixture was heated to 100 °C using microwave irradiation for 1 h. The THF was removed, and the Pd/C was filtered off over Celite®. The crude product was purified by chromatography on silica gel eluting with a gradient of hexane/EtOAc (Yield: 33 mg, 65%).

<sup>1</sup>H NMR (300 MHz, chloroform-*d*) δ 8.50 (d, *J* = 2.5 Hz, 1H), 8.44 (dd, *J* = 4.9, 1.8 Hz, 1H), 8.09 (s, 2H), 7.82 - 7.77 (m, 1H), 7.75 - 7.68 (m, 1H), 7.60 - 7.55 (m, 1H), 7.55 - 7.48 (m, 1H), 7.25 - 7.19 (m, 2H), 3.36 - 3.27 (m, 2H), 3.24 - 3.16 (m, 2H). LCMS: R<sub>t</sub> = 1.05 min; MS (ESIpos) *m/z* = 235.09 [M+H]<sup>+</sup>

#### Methyl 2-(1-(1*H*-benzo[d]imidazol-2-yl)-5-hydroxy-1*H*-pyrazol-3-yl)acetate.

Synthesis of the benzimidazole pyrazolone scaffold began with condensation of dimethyl-1,3-acetonedicarboxylates and 1*H*-1,3-benzimidazole-2-yl-hydrazines. After formation of an imine intermediate, cyclisation was initiated by heating in boiling ethanol to yield the benzimidazole pyrazolone product.<sup>3,4</sup>

## Novel Scaffold Inhibitor of KDM4 Enzymes

50 mg (0.34 mmol) of (1H-1,3-benzimidazol-2-yl)-hydrazine was solubilized in 4 ml EtOH. After addition of 50  $\mu$ l (0.34 mmol) of dimethyl-3-oxopentanedioate the mixture was heated to 80 °C for 1 h. The solvent was removed, and raw product was purified by HPLC eluting with a gradient of ACN/water (Yield: 16 mg, 17%).

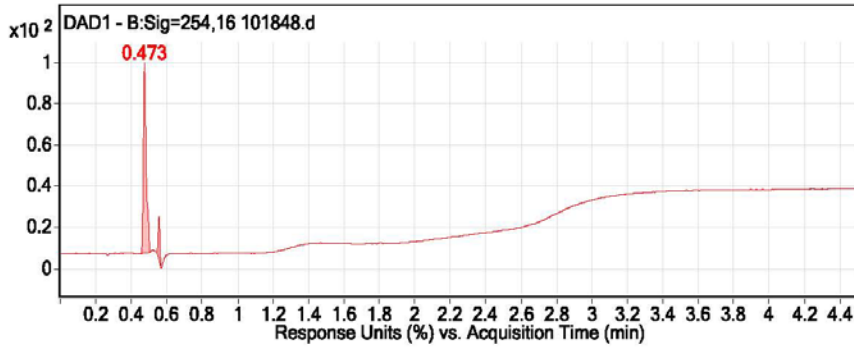
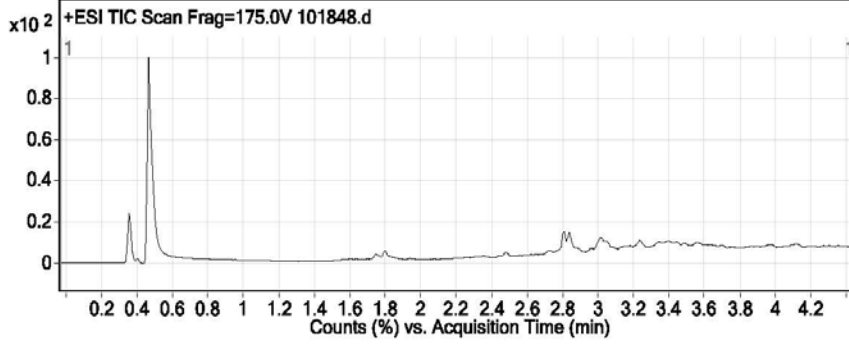
$^1\text{H}$  NMR (300 MHz, DMSO- $d_6$ )  $\delta$  7.51 (dd,  $J = 6.0, 3.2$  Hz, 2H), 7.16 (dd,  $J = 6.0, 3.2$  Hz, 2H), 5.24 (s, 1H), 3.64 (s, 3H), 3.59 (s, 2H). LCMS:  $R_t = 0.854$  min; MS (ESIpos)  $m/z = 273.2$   
[M+H] $^+$

# QC Data: CBN 101848

## Qualitative Analysis Report

### User Chromatograms

Fragmentor Voltage 175 Collision Energy 0 Ionization Mode ESI

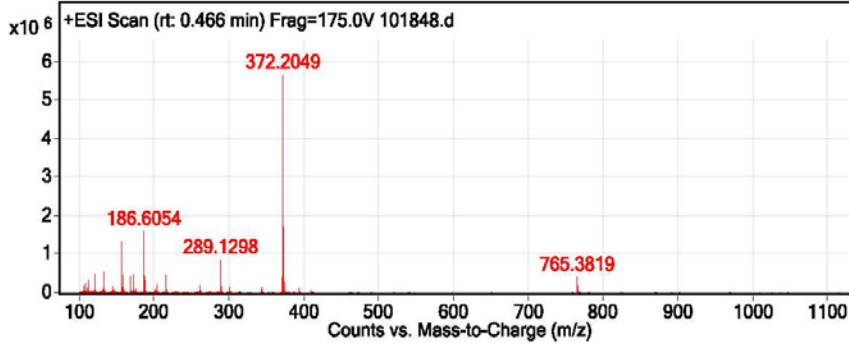


### Integration Peak List

Peak	Start	RT	End	Height	Area	Area %
1	0.452	0.473	0.507	25.05	28.34	100
2	0.543	0.557	0.567	5.75	3.66	12.92

### User Spectra

Fragmentor Voltage 175 Collision Energy 0 Ionization Mode ESI



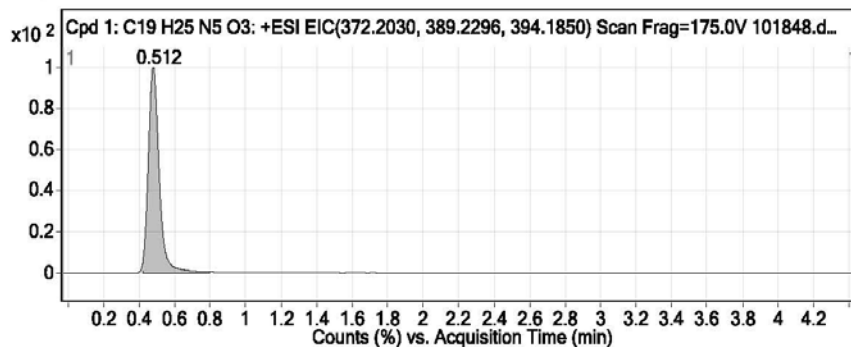
### Peak List

m/z	z	Abund
112.0393	1	332281.22
121.0762	1	478545.91

**Qualitative Analysis Report**

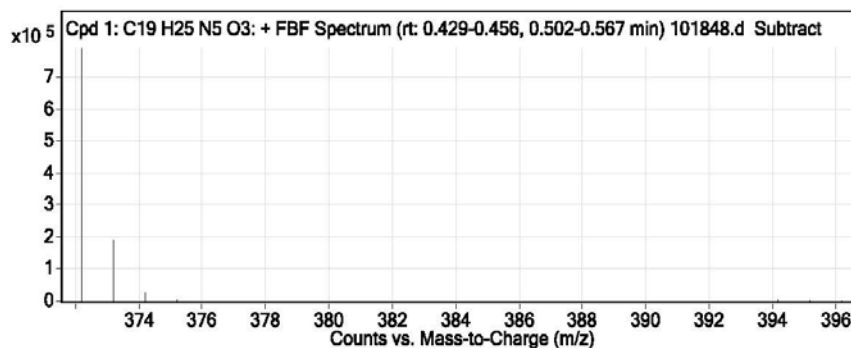
133.0762	1	543769.94
157.0608	1	1333710.13
159.0913	1	453218.25
169.0607	1	415468.13
172.0863	1	457274.22
186.6054	1	1586718.5
187.1081	1	445468.28
188.118	1	330446.28
216.1496	1	453575.69
289.1298	1	849924.31
371.1958	1	410247.44
372.2049	1	5653200.5
372.3637	1	459022.66
373.2064	1	1704311.13
765.3819	1	400762.66

**Compounds**



**Integration Peak List**

Start	RT	End	Height	Area
0.42	0.512	0.797	4381757	18807066



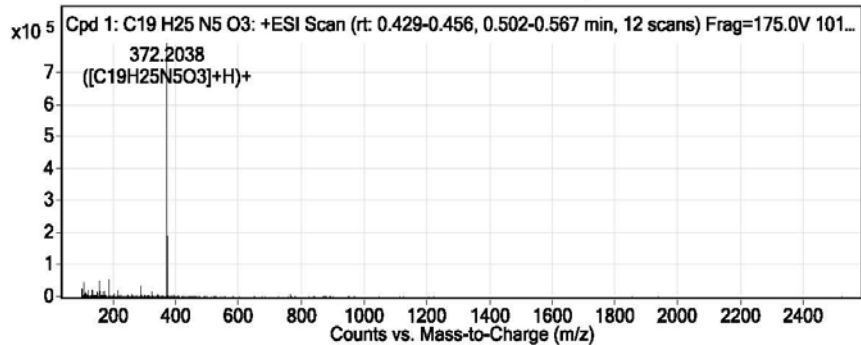
**Peak List**

m/z	z	Abund	Formula	Ion
372.2038	1	791032.88	C19H25N5O3	(M+H)+
373.2066	1	190579.41	C19H25N5O3	(M+H)+
374.2087	1	26189.48	C19H25N5O3	(M+H)+
375.2103	1	3157.48	C19H25N5O3	(M+H)+
394.1854	1	4247.89	C19H25N5O3	(M+Na)+
395.187	1	944.59	C19H25N5O3	(M+Na)+



### Qualitative Analysis Report

396.1876	1	99.64	C19H25N5O3	(M+Na)+
----------	---	-------	------------	---------



**Peak List**

m/z	z	Abund	Formula	Ion
372.2038	1	791032.88	C19H25N5O3	(M+H)+
373.2066	1	190579.41	C19H25N5O3	(M+H)+
374.2087	1	26189.48	C19H25N5O3	(M+H)+
375.2103	1	3157.48	C19H25N5O3	(M+H)+
394.1854	1	4247.89	C19H25N5O3	(M+Na)+
395.187	1	944.59	C19H25N5O3	(M+Na)+
396.1876	1	99.64	C19H25N5O3	(M+Na)+

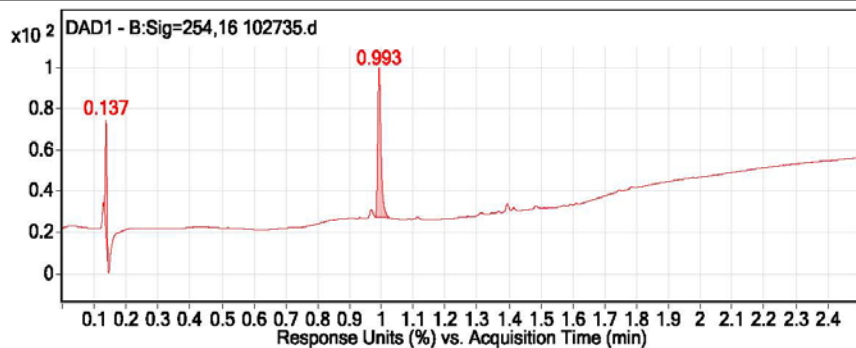
--- End Of Report ---

# QC Data: CBN 102735

## Qualitative Analysis Report

### User Chromatograms

Fragmentor Voltage 175 Collision Energy 0 Ionization Mode ESI

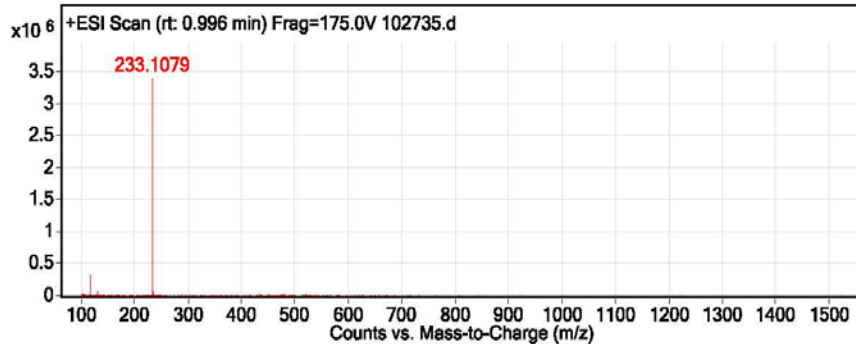


### Integration Peak List

Peak	Start	RT	End	Height	Area	Area %
1	0.131	0.137	0.143	15.14	5.3	37.85
2	0.981	0.993	1.028	19.55	13.99	100

### User Spectra

Fragmentor Voltage 175 Collision Energy 0 Ionization Mode ESI



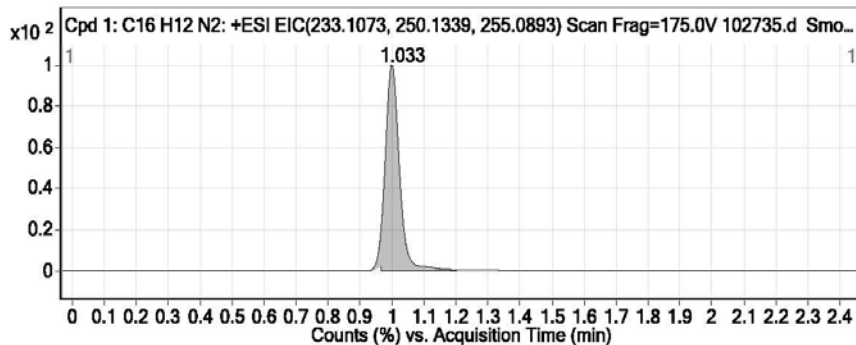
### Peak List

m/z	z	Abund
117.0574	1	325268.38
233.1079	1	3408436.25

### Qualitative Analysis Report

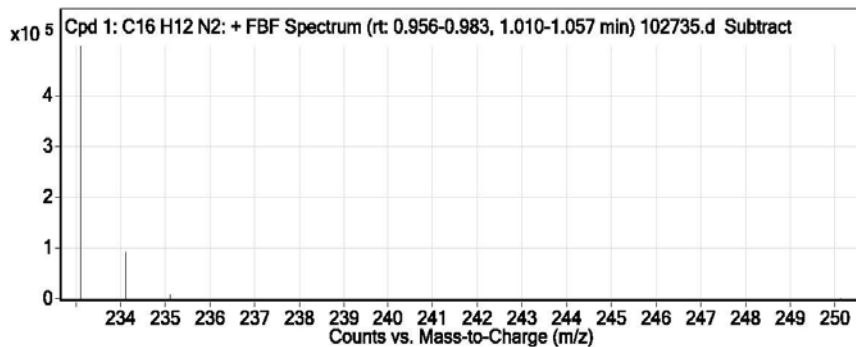
233.2375	1	288566.97
234.1101	1	750603.63

**Compounds**



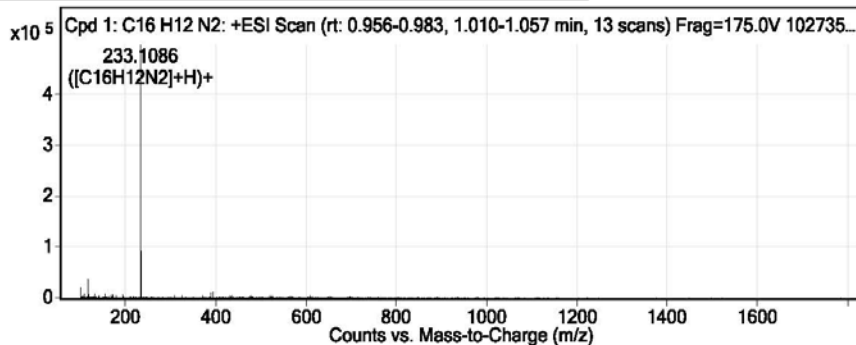
**Integration Peak List**

Start	RT	End	Height	Area
0.966	1.033	1.201	2068487	6461535



**Peak List**

m/z	z	Abund	Formula	Ion
233.1086	1	497665.97	C16H12N2	(M+H)+
234.1117	1	92346.55	C16H12N2	(M+H)+
235.1149	1	7710.58	C16H12N2	(M+H)+
250.1395	1	196.9	C16H12N2	(M+NH4)+



**Peak List**

### Qualitative Analysis Report

---

<i>m/z</i>	<i>z</i>	Abund	Formula	Ion
233.1086	1	497665.97	C16H12N2	(M+H)+
234.1117	1	92346.55	C16H12N2	(M+H)+
235.1149	1	7710.58	C16H12N2	(M+H)+
250.1395	1	196.9	C16H12N2	(M+NH4)+

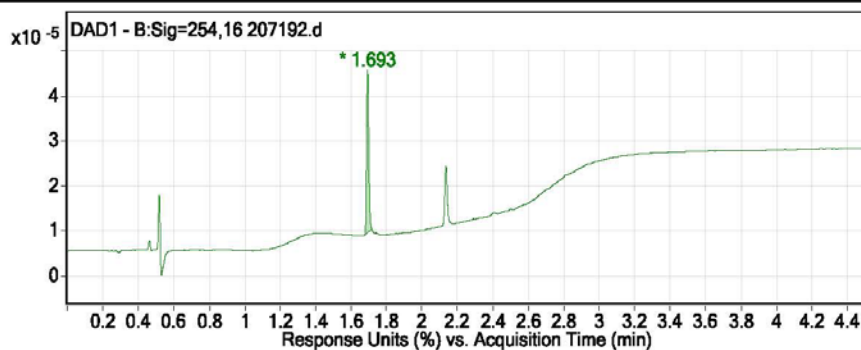
--- End Of Report ---

# QC Data: CBN 207192

## Qualitative Analysis Report

### User Chromatograms

Fragmentor Voltage 175 Collision Energy 0 Ionization Mode ESI

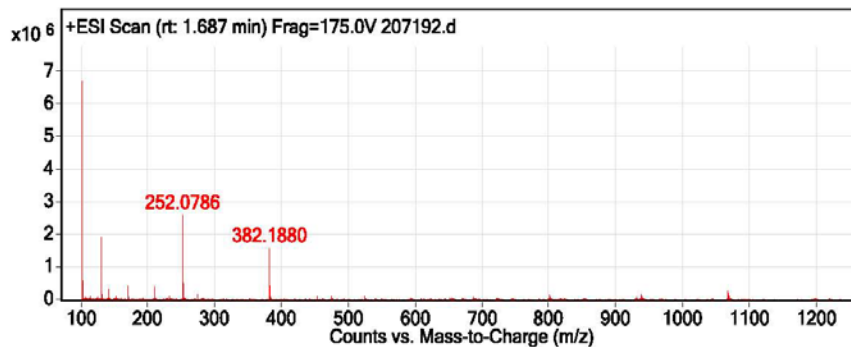


### Integration Peak List

Peak	Start	RT	End	Height	Area	Area %
1	1.675	1.693	1.717	14.46	12.21	100

### User Spectra

Fragmentor Voltage 175 Collision Energy 0 Ionization Mode ESI



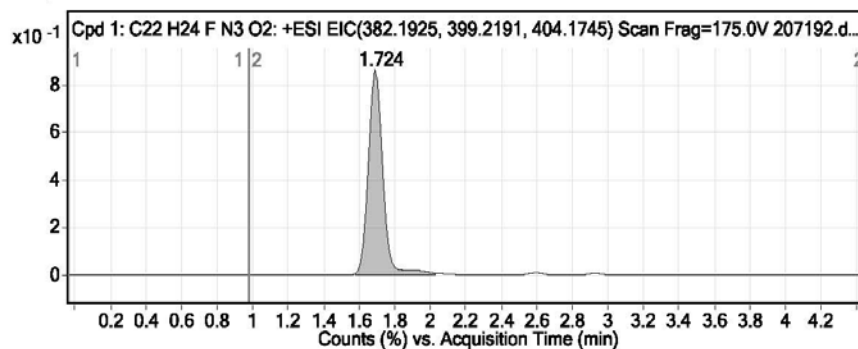
### Peak List

m/z	z	Abund
102.1269	1	6683509.5
102.2156	1	511573.47
103.1298	1	562610.63

### Qualitative Analysis Report

131.1161	1	1904861.63
170.1151	1	404643.53
210.1296	1	371307.03
252.0786	1	2570563.75
253.082	1	481230.16
382.188	1	1557637.63
383.1909	1	411579.09

**Compounds**



**Integration Peak List**

Start	RT	End	Height	Area
1.579	1.724	2.03	346289	1963465

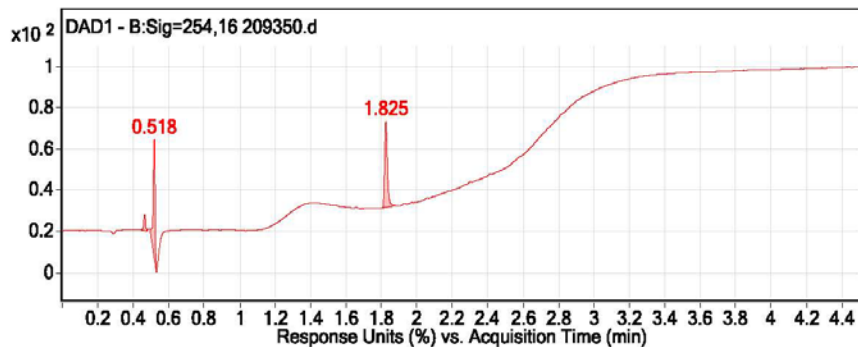
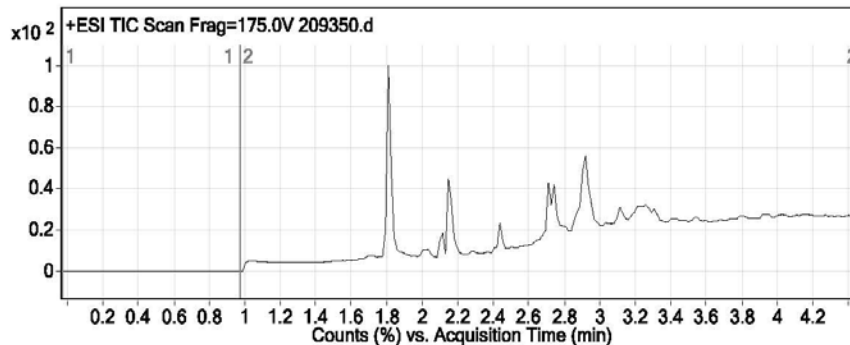
--- End Of Report ---

# QC Data: CBN 209350

## Qualitative Analysis Report

### User Chromatograms

Fragmentor Voltage 175 Collision Energy 0 Ionization Mode ESI

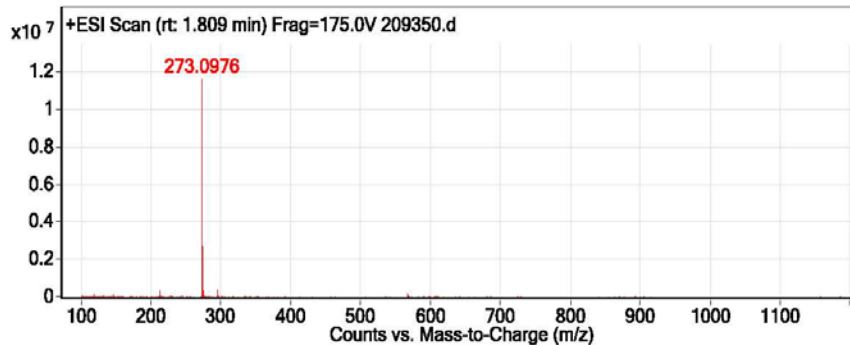


### Integration Peak List

Peak	Start	RT	End	Height	Area	Area %
1	0.433	0.463	0.475	0.86	0.63	12.16
2	0.493	0.518	0.53	6.44	4.73	92
3	1.803	1.825	1.882	4.66	5.14	100

### User Spectra

Fragmentor Voltage 175 Collision Energy 0 Ionization Mode ESI



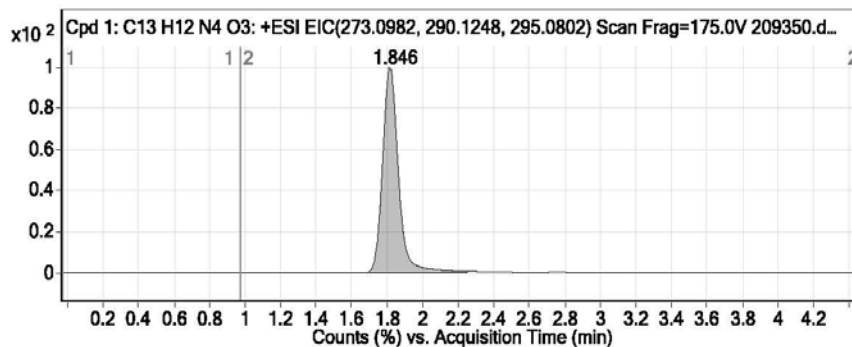
### Peak List

m/z	z	Abund
273.0976	1	11600180

**Qualitative Analysis Report**

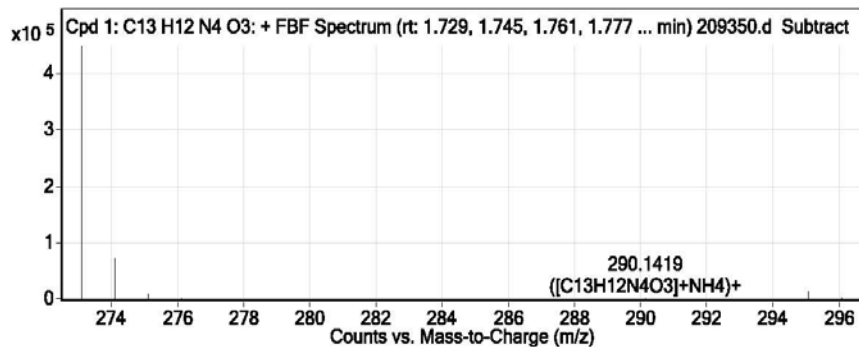
273.2352	1	1003582.13
274.099	1	2708185.25

**Compounds**



**Integration Peak List**

Start	RT	End	Height	Area
1.702	1.846	2.249	3915435	24394391

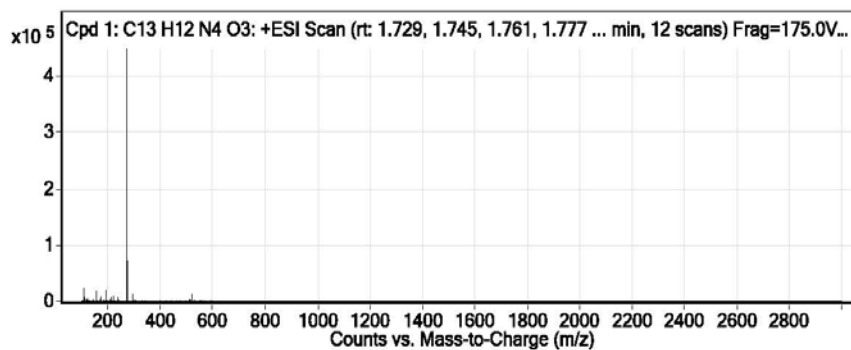


**Peak List**

m/z	z	Abund	Formula	Ion
273.0974	1	448960.31	C13H12N4O3	(M+H)+
274.1	1	72445.71	C13H12N4O3	(M+H)+
275.1023	1	8324.9	C13H12N4O3	(M+H)+
276.1071	1	627.84	C13H12N4O3	(M+H)+
290.1419	1	151.64	C13H12N4O3	(M+NH4)+
295.0789	1	14052.01	C13H12N4O3	(M+Na)+
296.0826	1	2259.89	C13H12N4O3	(M+Na)+



### Qualitative Analysis Report



Peak List

m/z	z	Abund	Formula	Ion
273.0974	1	448960.31	C13H12N4O3	(M+H)+
274.1	1	72445.71	C13H12N4O3	(M+H)+
275.1023	1	8324.9	C13H12N4O3	(M+H)+
276.1071	1	627.84	C13H12N4O3	(M+H)+
290.1419	1	151.64	C13H12N4O3	(M+NH4)+
295.0789	1	14052.01	C13H12N4O3	(M+Na)+
296.0826	1	2259.89	C13H12N4O3	(M+Na)+

--- End Of Report ---

### Supplemental References

1. Krasnov, K. A.; Kartsev, V. G. Synthesis of Spiroheterocyclic Systems from Barbituric Acids and N,N-Disubstituted O-Aminobenzaldehydes. *Russ. J. Org. Chem.* **2005**, *41*, 901–906.
2. Thinnes, C. C.; Tumber, A.; Yapp, C.; et al. Betti Reaction Enables Efficient Synthesis of 8-Hydroxyquinoline Inhibitors of 2-Oxoglutarate Oxygenases. *Chem. Commun.* **2015**, *51*, 15458–15461.
3. Povstyanoy, V. M. et al. Synthesis of Substituted 2- Pyrazolylbenzimidazoles and 1,2,4-Triazepino and 1,2,4-triazino[4,3-A]benzimidazoles from 2-Hydrazino(alkylhydrazino)benzimidazoles and 1,3-Difunctional Compounds. *J. Org. Pharm. Chem.* **2005**, *3*, 32–37.
4. Stanovnik, B.; Bevk, D.; Jakse, R.; et al. Transformations of Alykl (5-Oxo-1-Phenyl-4,5-Dihydro-1H-Pyrazol-3-Yl)acetates into 5-Heteroaryl-3-Oxo-2-Phenyl-3,5-Dihydro-2H-pyrazolo[4,3-C]pyridine-7-Carboxylates. *Heterocycles* **2003**, *61*, 197–223.
5. Kouznetsov, V. V.; Meléndez Gómez, C. M.; Derita, M. G.; et al. Synthesis and Antifungal Activity of Diverse C-2 Pyridinyl and Pyridinylvinyl Substituted Quinolines. *Bioorg. Med. Chem.* **2012**, *20*, 6506–6512.
6. Ogata, Y.; Kawasaki, A.; Hirata, H. Condensation of 2-Methylquinoline with Benzaldehydes in Acetic Anhydride. *J. Chem. Soc. Perkin Trans. 2* **1972**, *9*, 1120–1124.